



# Geomechanical Field Survey to Identify an Unstable Rock Slope: The Passo della Morte Case History (NE Italy)

Alberto Bolla<sup>1</sup> · Paolo Paronuzzi<sup>1</sup>

Received: 12 April 2019 / Accepted: 1 September 2019 / Published online: 24 October 2019  
© Springer-Verlag GmbH Austria, part of Springer Nature 2019

## Abstract

In this work, a geomechanical study performed on a natural rock slope located in north-eastern Italy (Tagliamento River valley, Friuli Venezia Giulia Region) is presented. The detailed geomechanical survey has provided a large bulk of field data proving that the investigated limestone slope is characterized by strong rock mass damage, thus resulting in a critical stability condition. Field evidence includes: (1) local faults crossing the rock mass and representing internal sliding surfaces; (2) slickensides and fault slips within the rock mass; (3) fracture joints of gravity-induced origin; (4) strong rock mass damage in over-stressed zones of the slope; and (5) slope monitoring data recorded by some installed devices. Three failure scenarios have been identified: a wedge failure involving a limestone block of 110,000 m<sup>3</sup> (failure scenario 1: BLOCK1); a larger wedge failure involving an assembled limestone block of 200,000 m<sup>3</sup> (failure scenario 2: BLOCK1-2-3); and a retrogressive failure involving a rear dolomitic block possibly triggered by the collapse of the limestone slope, mobilizing a maximum volume of 335,000 m<sup>3</sup> (failure scenario 3: DOLOMITIC BLOCK). This paper shows that to comprehensively study stability problems involving natural rock slopes we must consider the interaction between pre-existing discontinuities, internal sub-blocks subdividing the unstable slope, rock mass strength and gravity-induced fractures that form during the delicate phase preceding slope collapse. Gravity-induced joints can be differentiated on the field from those of tectonic origin on the basis of some geometrical features, in particular their lower persistence and higher joint roughness.

**Keywords** Rock slope · Field survey · Wedge failure · Rock mass damage · Gravity-induced fracturing · Progressive failure

## 1 Introduction

Rockslides can originate risk situations causing serious threat to people, inhabited areas, communication lines and infrastructures located in mountainous regions of various climatic environments around the world (Abele 1974). In common practice of risk management and mitigation, both researchers and professional technicians are increasingly called upon to analyze and predict the stability of a given slope, assessing its risk, potential failure mechanisms, areas endangered, and possible remedial measures (Eberhardt 2003). To properly address these features, it is essential to understand the complex mechanical processes that affect the unstable rock slope and which can lead to the eventual

collapse. Consequently, rock slope stability problems often require studies aimed at recognizing processes and underlying mechanisms driving the instability, including progressive fracturing and/or deformation involving the unstable rock mass prior to slope collapse.

Rock mass damage features related to the progressive failure of rock slopes include: newly formed fractures, joint opening, disintegrated and/or pulverized rocks, brittle folds, internal sliding surfaces, cataclastic bands, differential block movements, etc. (Chigira 1992; Jaboyedoff et al. 2013; Paronuzzi and Bolla 2015a). The identification of the above-mentioned geomechanical clues is decisive in understanding the processes driving the instability and requires a detailed field survey of the investigated slope area. Field evidence of rock mass damage is more frequently reported in a posteriori studies of rockslides. This essentially occurs through a field survey of the detachment surface and, specifically for block slides, of the failed rock mass (Chang et al. 2005; Eberhardt et al. 2005; Brideau et al. 2006; Chigira 2009; Tsou et al. 2011; Paronuzzi and Bolla 2012, 2015a; Sturzenegger and

✉ Alberto Bolla  
alberto.bolla@uniud.it

<sup>1</sup> Dipartimento Politecnico di Ingegneria e Architettura,  
Università degli Studi di Udine, via Cotonificio 114,  
33100 Udine, Italy

Stead 2012; Paronuzzi et al. 2016a; Sandøy et al. 2017). On the contrary, geomechanical evidence of rock mass damage affecting unstable rock slopes susceptible to failure has rarely been described and discussed in literature (Deng et al. 2000; Braathen et al. 2004; Agliardi et al. 2013; Bolla and Paronuzzi 2017). In a priori analyses of rock slopes prone to failure, the mechanical behavior of the slope and the related failure mechanisms are typically evaluated through data obtained from: remote sensing (photogrammetry, laser scan, interferometry), monitoring of surface and deep slope displacements, geophysical surveys (ground penetrating radar, seismic reflection and refraction, acoustic emission), boreholes, pore pressure measurements, geomorphological and structural mapping, rock discontinuity and rock mass characterization, etc. (Bonzanigo et al. 2007; Ganerød et al. 2008; Willenberg et al. 2008a, b; Barla et al. 2010; Zangerl et al. 2010; Brideau et al. 2011; Gigli et al. 2011; Cloutier et al. 2016; Tomás et al. 2018). However, this data is rarely compared with mechanical indicators of rock mass damage that can actually be recognized on the field.

This discrepancy is mainly due to the scarce amount of information about field evidence associated with progressive rock mass damage involving unstable rock slopes susceptible to failure. The determining preparatory mechanical processes leading to slope collapse are difficult to detect both practically and conceptually. Unstable slopes with a prevailing rigid behavior, such as igneous rocks and massive sedimentary rocks, very often exhibit small-sized field evidence that proves progressive deformation/fracturing of the rock mass (Paronuzzi et al. 2016b). In addition, newly formed fractures are difficult to identify on the field and it is not simple to differentiate these gravity-induced fractures from the pre-existing joints of tectonic origin (Paronuzzi and Bolla 2015a, b). For these reasons, gravity-induced fractures often remain undetected.

In addition, the attention is still conceptually focused on the slope rupture condition, this being a consequence of the widely used Limit Equilibrium Method (LEM). However, owing to its rigid block assumption, the LEM cannot account for the complex mechanical processes of internal rock mass damage involving most rock slope failures (Eberhardt 2003). Another conceptual difficulty lies in the “geological” nature of preparatory mechanical processes. These long-term processes (with duration from 1000–2000 years to 10,000–20,000 years) are strongly influenced by climatic-controlled events such as the rapid deglaciation of the Alpine valleys (Abele 1974; Holm et al. 2004; Cossart et al. 2008). Comprehensive understanding of the crucial phenomenon controlling pre-collapse slope behavior requires an integrated approach including: (1) the reconstruction of major late Pleistocene–Holocene geological events; (2) the acquisition of detailed field data; (3) the evaluation of slope monitoring data (wherever possible); and (4) the analysis of the

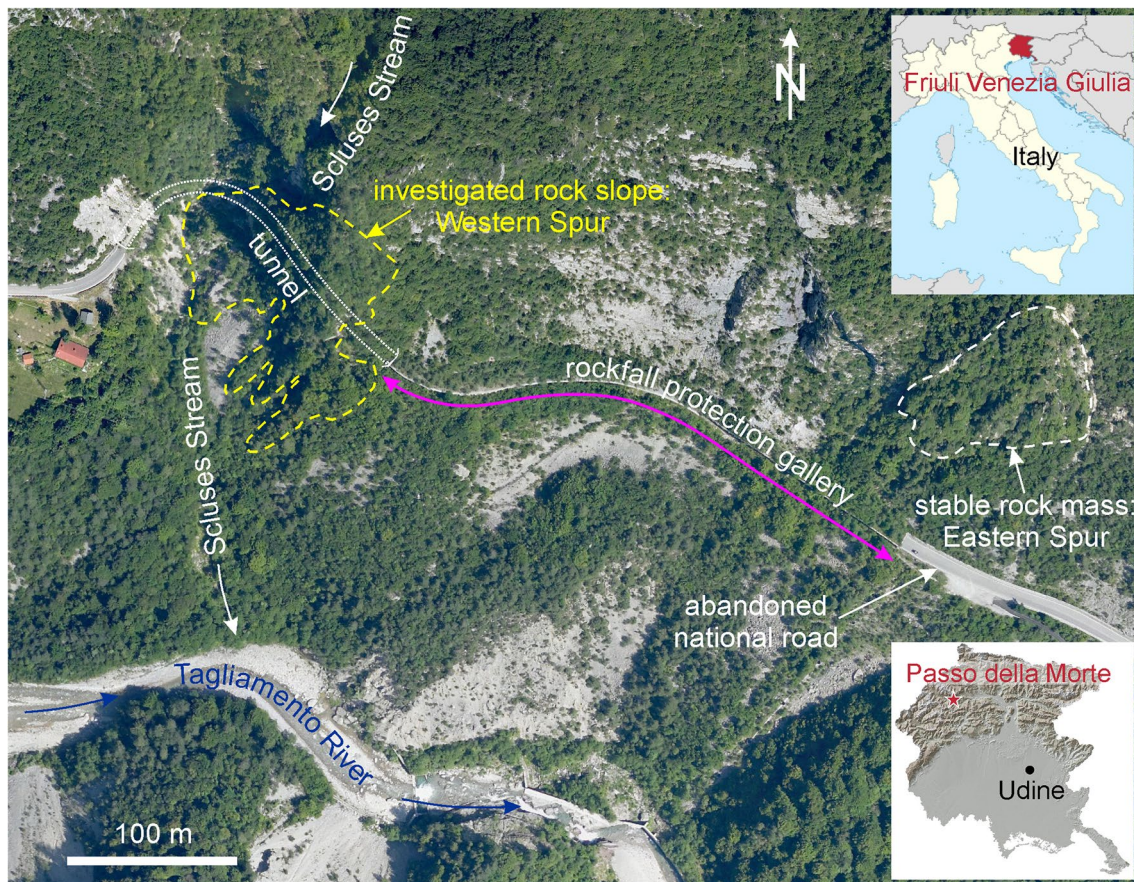
mechanical indicators of rock mass damage obtained from the stress–strain modeling of the unstable slope. Numerical modeling applied to rock slope stability problems can be very effective in providing key insights into the mechanical processes of progressive damage involving unstable slopes before collapse (Eberhardt 2008).

In this work, we present a geomechanical study that was performed on a natural rock slope located in north-eastern Italy (Tagliamento River valley, Friuli Venezia Giulia Region, Fig. 1). It was aimed at investigating the stability condition and potential failure mechanism of the slope. A field survey has been carried out in order to identify possible geomechanical evidence of rock mass damage related to the progressive failure of the slope. The extensive geomechanical evidence recognized on the field, as well as the slope monitoring data available, allowed us to explore the rock mass damage process involving unstable slopes approaching failure condition. Field evidence also led to the assessment of an engineering–geological model of the investigated slope. This model was subsequently implemented into slope stability analyses. In a separate paper (Bolla and Paronuzzi, submitted), we present the results of a 2D and 3D numerical modeling of the investigated slope aimed at analyzing its stress–strain behavior and internal rock mass damage. In that paper, we also compared the mechanical indicators of rock mass damage obtained from the numerical analyses with actual damage features recognized on the slope.

## 2 Materials and Methods

The main aim of this work was the assessment of geomechanical evidence of rock mass damage that affects an unstable rock slope during the delicate phase preceding slope collapse. Field evidence is based on the integration of the data acquired from (1) a geological and geomechanical field survey; (2) photographic documentation acquired in situ; (3) digital terrain model; (4) slope monitoring.

The field survey was performed on the investigated slope, as well as on the surrounding area, to properly assess the geological context in which the slope is located. The geomechanical survey provided information on the structural arrangement of the rock masses, on the orientation of rock discontinuities, and on the mechanical characteristics of both the intact rock and the rock masses. Field data were acquired from many different outcrops within the study area in order to understand local variations in the characteristics of the rock mass. A large amount ( $N=1108$ ) of orientation data of bedding planes and fracture joints was collected. In addition, structural and kinematic data were also acquired from folded and faulted rock layers as well as from striated surfaces. Orientation data of the geologic structures will be



**Fig. 1** Orthophoto (year 2007) of the study area located along the Tagliamento River valley. The investigated slope at the ‘Passo della Morte’ site is highlighted

presented throughout the paper according to the ‘dip direction/dip’ notation.

Many rock surfaces were tested using the Schmidt hammer (both type L and type N) in order to evaluate the compressive strength of the joint surfaces as well as of the intact rock (total number of impacts:  $N=2860$ ). Some joint surfaces were also characterized using the Barton–Bandis shear strength criterion (Barton and Choubey 1977; Barton and Bandis 1990) in order to evaluate their peak friction angle. Rock mass characteristics and intact rock properties were then employed for the mechanical characterization of the rock masses, according to the Hoek and Brown procedure (Hoek 2007).

The examination of the photographic documentation taken on the field allowed for the recognition of some important damage features that characterize the rock mass. In many cases, photos were used to schematize the rock mass arrangement, identifying field evidence of internal damage. Morphological features of the investigated slope and of the surrounding area were defined by means of a specific orthophoto (Fig. 1) and a Digital Terrain Model (Fig. 2), both provided by the Civil Protection of the Friuli

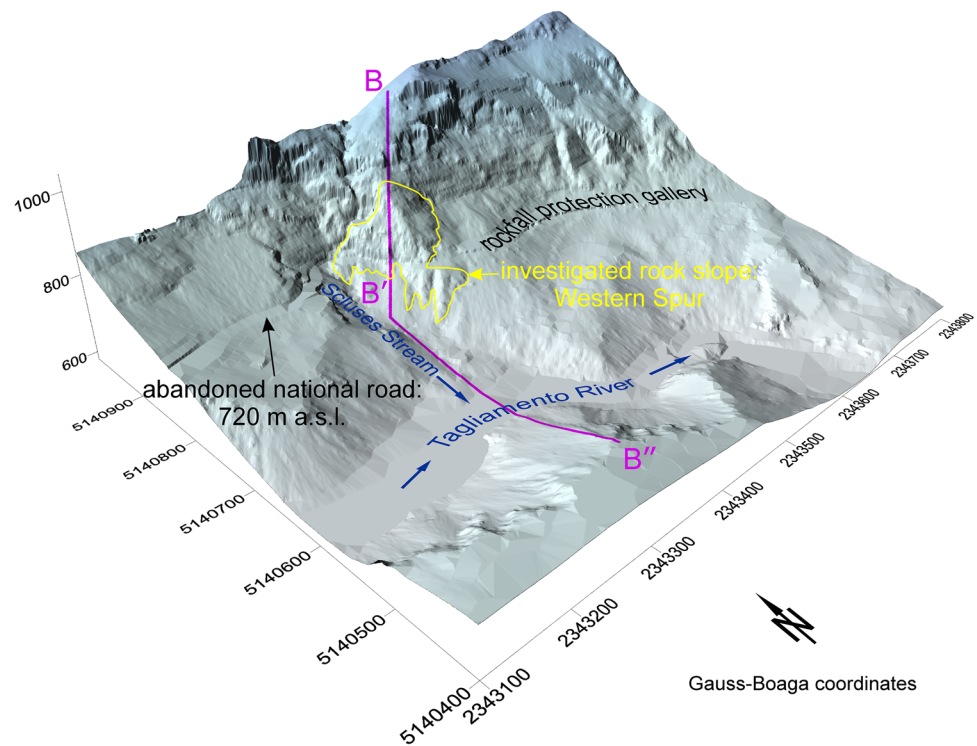
Venezia Giulia Region. The original scale (data density: 4 points per  $m^2$ ) resulted in a good representation of the main slope geometry. The DTM was also used to reconstruct the 3D geometry of the various blocks forming the rock mass and to draw the reference geological cross section of the slope.

The investigated slope had been monitored in the past by means of several devices that were installed by the Research Institute for Geo-Hydrological Protection of the Italian National Research Council (IRPI-CNR) on behalf of the Civil Protection of the Friuli Venezia Giulia Region. The data available provided us with useful information on surface and deep slope displacements, groundwater level variations, and acoustic emissions.

All field data were used to establish an engineering–geological model of the investigated slope. This geomechanical model was defined on the basis of the following issues:

- determination of the morphological and geological context of the study area;
- reconstruction of the structural arrangement of the slope and of the surrounding rock masses;

**Fig. 2** Three-dimensional surface view (DTM data density: 4 points per  $m^2$ ) of the Passo della Morte area. The reference geological cross section B–B'' is also shown



- identification of the potential failure surfaces delimiting unstable rock blocks;
- evaluation of the volume of the rock blocks susceptible to failure;
- identification of the kinematics of the unstable blocks.

A preliminary evaluation of the stability condition of the investigated slope has also been advanced, along with the identification of three different failure scenarios.

### 3 The Passo della Morte Slope

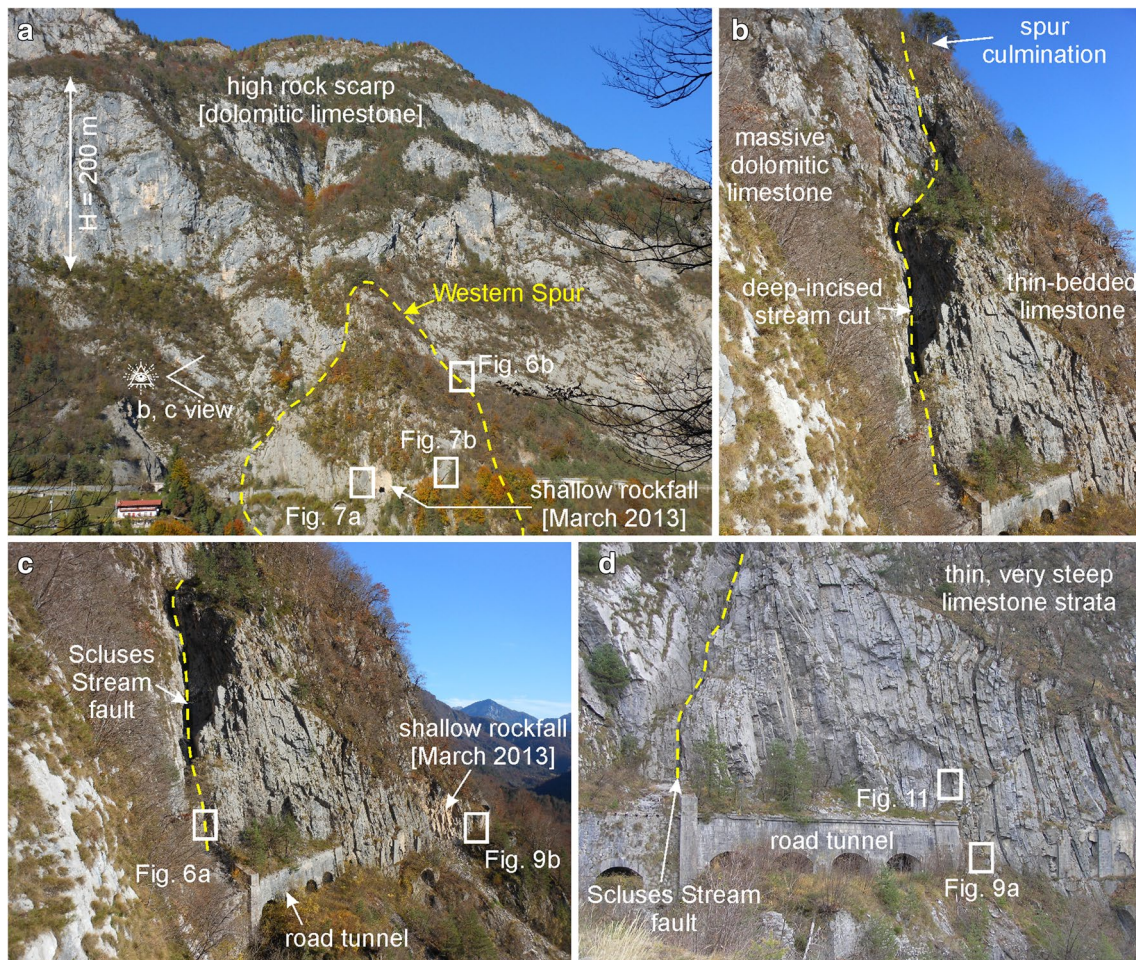
The study area is located in the Carnic Alps, in the Municipality of Forni di Sotto (Friuli Venezia Giulia Region, NE Italy), along the mountainous stretch of the Tagliamento River valley (Fig. 1). The investigated slope is located on the left (north) side of the valley in a site named 'Passo della Morte' (Figs. 1, 2), and is crossed by a rock tunnel related to an abandoned national road ('SS 52 Carnica').

#### 3.1 Geomorphology

At the Passo della Morte site the Tagliamento River valley is deeply incised (Figs. 1, 2). The north valley side is dominated by a large mountain range with some peaks up to 2100 m a.s.l. and several very steep and high rock scarps ( $H=50\text{--}200$  m; Figs. 2, 3). These scarps are made up of massive dolomitic limestone (bed thickness: 100–300 cm

and are 1–5 km long, with a prevailing ESE–WNW trend (Fig. 4). Compared with this quite regular arrangement, the investigated slope shows a marked morphological contrast. The slope is characterized by a particular pyramidal geometry giving it the shape of a spur, thus emphasizing a morphological relief in relation to the continuous strip of rock scarps resting behind it (Figs. 3, 4). For this geometrical peculiarity, the investigated slope has been named 'Western Spur' in this study (WS in Fig. 4). The Western Spur is completely formed of highly tilted and thinly stratified limestone (bed thickness: 10–30 cm, on average).

This large rock pyramid is defined by two main slope faces (Figs. 1, 2): a western one, extended farther and mainly dipping towards the SW, and an eastern one, of a smaller size and dipping towards the SSE. The average slope height is about 150 m, extending from 700 m a.s.l. to 850 m a.s.l. in correspondence to the spur culmination (Fig. 3). A debris cone made up of limestone blocks and slabs extends from the base of the rock spur towards the valley bottom. The presence of a coarse slope deposit proves the occurrence of past rockfalls (mainly surface toppling and buckling failures). A shallow rockfall occurred on March 2013 and involved a small rock mass (volume  $200\text{ m}^3$ ) located in the frontal-toe part of the limestone spur (Figs. 3, 5). The Western Spur is bounded at its western limit by the vertically incised stream cut created by the 'Scloses' Stream (Fig. 2). The Scloses Stream is an ephemeral stream that steeply flows from the high dolomitic scarps (Fig. 3a) and then abruptly turns towards the



**Fig. 3** The investigated rock slope: **a** frontal view from the opposite valley side; **b, c** lateral views showing the abrupt limit between the limestone spur and the rear dolomitic rock slope; **d** detail of the western scarp of the limestone spur

west flowing at the contact between the dolomitic cliffs and the limestone spur (Fig. 3b, c).

A very similar geometrical configuration characterizes the slope on the north valley side some hundreds of meters to the east, just above the eastern entrance of the rockfall protection gallery (Figs. 1, 4). Here, another rock spur formed by thin-bedded limestone is in contact with the rear dolomitic scarps. Owing to these similarities, this rock polyhedron has been named ‘Eastern Spur’ in this study (ES in Fig. 4).

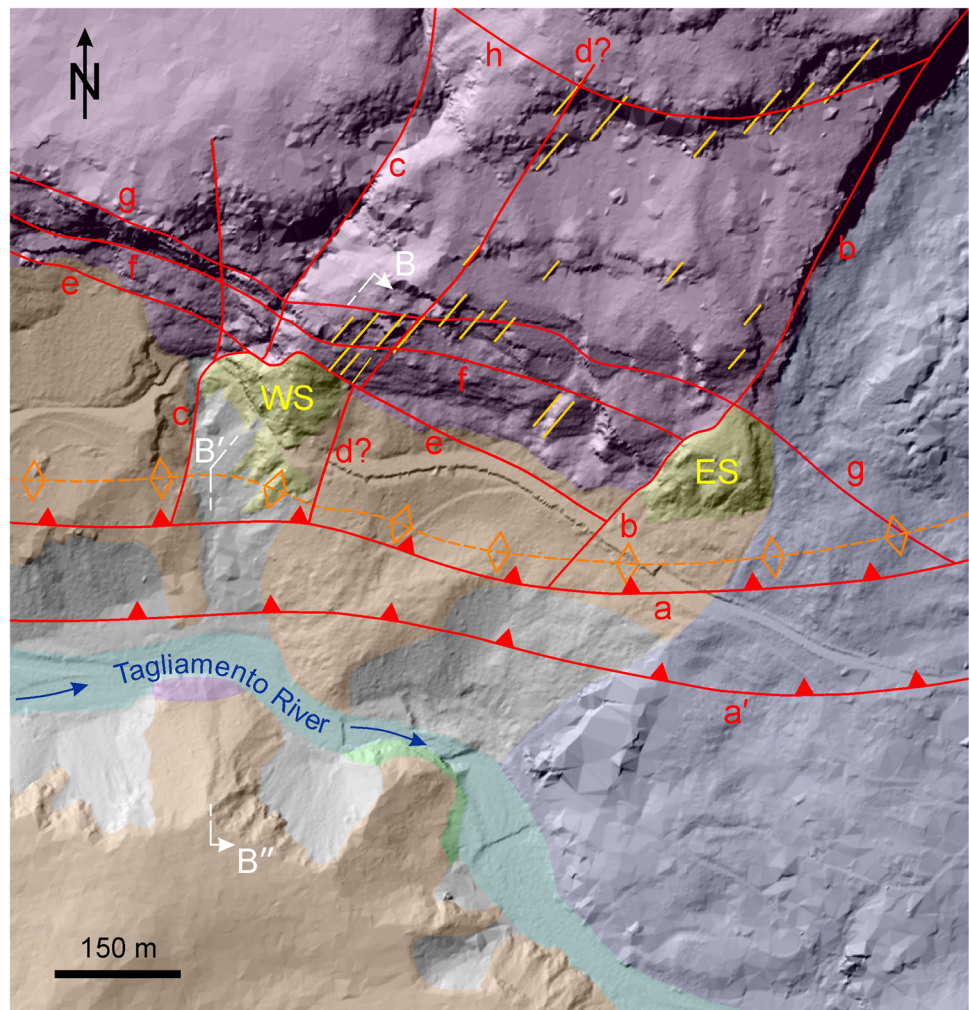
The current morphology of the valley slopes is the result of the geomorphologic processes that affected this stretch of the Tagliamento valley during the Pleistocene and Holocene ages (Pisa 1972; Martinis 1985). A number of landslides occurred in the study area and some deep-seated gravitational slope deformations are still active (Fig. 4). The ‘Clap di Lavres’ rockslide (volume 40 million m<sup>3</sup>) was a large slope failure that occurred prior to 9970 years BP (Martinis 1994). This prehistoric rockslide involved the

southern slopes of the mount ‘Clap di Lavres’, which is located upslope of the Passo della Morte, and originated a huge slide mass that dammed the Tagliamento River, thus creating a landslide dam lake that probably lasted 200 years (Martinis 1994). The subsequent erosion of the Tagliamento River across the failed mass determined the current deeply incised morphology of the valley with the landslide deposit resting on both valley sides (Figs. 4, 5). The Western Spur is located at the lower extremity of a tight mountain ridge that clearly separates two areas involved in the Clap di Lavres landslide (Fig. 4).


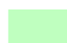










### 3.2 Geology

The lithostratigraphical sequence characterizing the study area includes the geological formations of Triassic age listed in Table 1 (Pisa 1972; Carulli 2006). The ‘Dolomia dello Schlern’ Fm. and the ‘Calcarì Scuri’ Fm. are the only geological formations that outcrop at the Passo della Morte site

**Fig. 4** Tectonic sketch map showing the major faults and folds occurring in the Passo della Morte area. a: ‘Tagliamento Valley’ overthrust; a’: subsidiary of the ‘Tagliamento Valley’ overthrust; b: ‘Mount Tinisa’ fault; c: ‘Scloses Stream’ fault; d: subsidiary of the ‘Scloses Stream’ fault; e: ‘Passo della Morte’ fault; f: ‘Caprera’ fault; g: ‘San Lorenzo’ fault; h: ‘Clap di Lavres’ fault. The locations of both the Western Spur (WS) and the Eastern Spur (ES) are highlighted



#### LEGEND

 fluvial deposit	 Argille siltose varicolori Fm.	 master joint
 active debris	 limestones and stratified dolostones	 overthrust
 prehistoric slide deposit [Clap di Lavres landside]	 Calcari Scuri Fm.	 anticline
 Deep seated gravitational slope deformation	 Dolomia dello Schlern Fm.	 fault

(Figs. 4, 5). The Passo della Morte slope is located in an Alpine valley affected by a complex tectonic framework. Some important tectonic structures affecting the study area were recognized by previous studies at both a regional and local scale (Pisa 1972; Carulli 2006). Nonetheless, the field survey carried out in the study area helped define the tectonic framework in the surroundings of the investigated slope.

The major faults and folds characterizing the study area are shown in Fig. 4. The most relevant geological discontinuity of the area is the ‘Tagliamento Valley’ overthrust (a in Fig. 4). This E–W trending, south-vergent thrust caused

the thrusting of the thick and more rigid sequence formed by the Dolomia dello Schlern and Calcari Scuri formations over the more ductile sequence formed by the lithostratigraphical units belonging to the Middle and Upper Carnian age (Arenarie Violette Fm.–Argille siltose varicolori Fm.) (Fig. 5). The rock layers on the north valley side are arranged in the form of an anticline fold with a low-angle axial plane (Figs. 4, 5). The Tagliamento Valley overthrust is probably accompanied by a subsidiary structure (a’ in Fig. 4) that caused a doubling of the lower, more ductile sequence (Fig. 5).

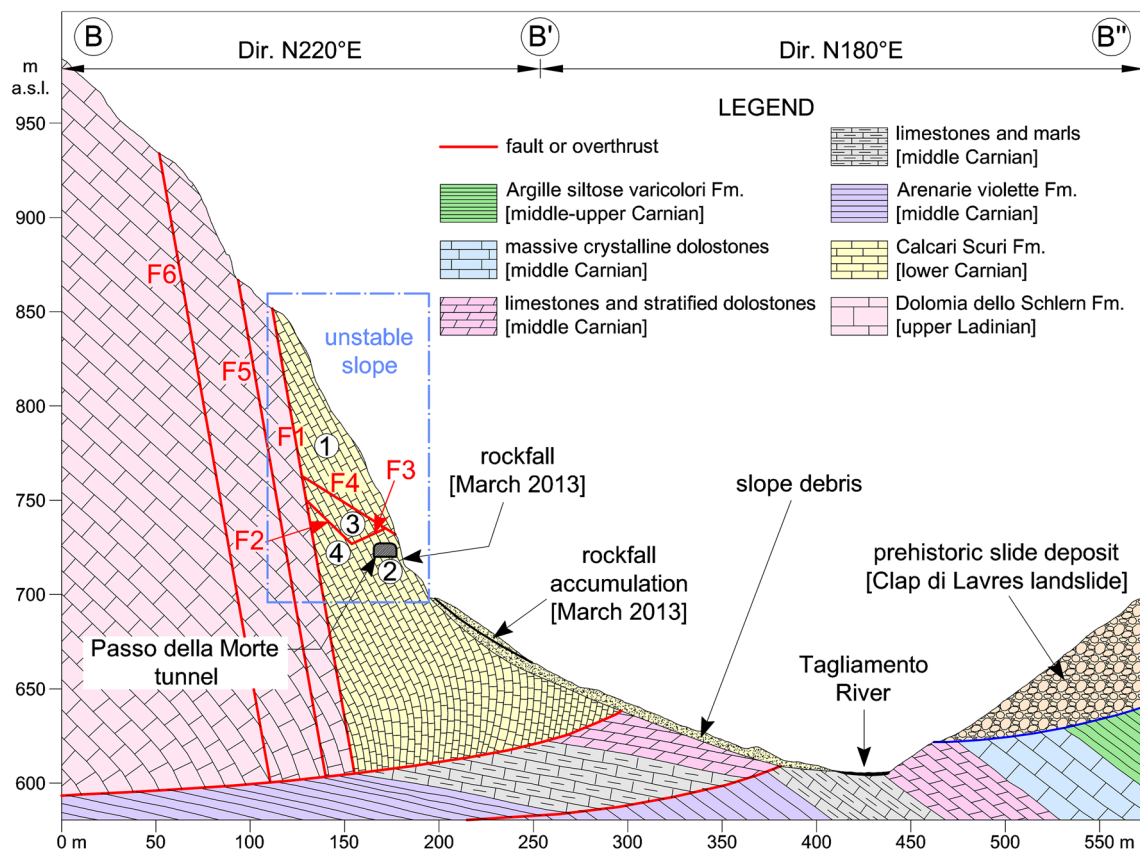


Fig. 5 Reference geological section B–B'' across the Passo della Morte slope. See Fig. 2 for the cross-section location

Table 1 Lithological features of the geological formations outcropping in the study area, from the top to the bottom

Geological formation	Age	Lithological description	Thickness (m)
'Argille siltose varicolori'	Middle–Upper Carnian	Thinly laminated claystones, silty claystones and siltstones with variable colors. Some fine-grained, grayish marly dolostones are present	80–85
massive crystalline dolostones	Middle Carnian	Coarse-grained, gray and light gray crystalline dolostones (content of dolomite > 95%), in massive layers	75–80
limestones and stratified dolostones	Middle Carnian	Coarse-grained, crystalline limestones and dark gray, fine-grained saccharoid dolostones with very thin stratification (4–10 cm)	20–25
limestones and marls	Middle Carnian	Close and irregular alternation of thin-stratified (5–25 cm) dark limestones, fine-grained dolomitic limestones, marly limestones, marls, and fine-grained sandstones	30–35
'Arenarie violette'	Middle Carnian	Violet, reddish and greenish quartz and feldspathic sandstones, from coarse- to fine-grained, alternated with silty claystones, dolostones and marly dolostones. Generally very thinly stratified (5–30 cm), but some massive layers (100–200 cm) are present	90–110
'Calcarei Scuri'	Lower Carnian	Dark gray, black limestone, often fossilized, very fine-grained with frequent veins of calcite. Frequent layers and nodules of chert. The stratification is planar or undulated and generally thin (10–30 cm), but some thick layers occur (50–100 cm). Marly interbeds occasionally occur (thickness 2–30 cm)	90–100
'Dolomia dello Schlern'	Upper Ladinian	Gray, light brown and whitish dolostone and dolomitic limestone, highly crystallized and sometimes closely laminated. Generally massively stratified (100–300 cm), but some closely stratified (40–100 cm) and planar layers are present in the upper part of the formation	270–300

The study area is affected by two main groups of sub-vertical or high-angle faults with two prevailing directions that are mutually orthogonal to each other. The first group of faults has a NNE–SSW direction (b–d in Fig. 4), whereas the second group of faults is characterized by a ESE–WNW direction (e–h in Fig. 4). Some of these faults are key because they partially delimit the Passo della Morte slope. The ‘Scluses Stream’ fault (c in Fig. 4) and the ‘Passo della Morte’ fault (e in Fig. 4) intersect each other and put the thin-bedded limestone of the Western Spur and the rear dolomitic scarps into contact, thus completely delimiting the limestone slope at its back (Figs. 3, 4). The Scluses Stream fault (dip dir./dip: 165/90) runs along the deep-incised cut created by the homonymous stream (Fig. 3) and is characterized by the presence of a thick layer (50–100 cm) of crushed and locally re-cemented limestone (Fig. 6a).

The Passo della Morte fault (205/80; F1 in Fig. 5) is a rather long, transcurrent fault, with a right-lateral motion. It has been identified both to the east and to the west of the Western Spur. During the field survey, several fault surfaces, slickensides and tectonic breccias have been recognized (Fig. 6b). Owing to their intersection, the Passo della Morte and Scluses Stream faults represent possible rear detachment surfaces for potentially unstable rock masses belonging to the Western Spur. The ‘Caprera’ fault (f in Fig. 4 and F5 in Fig. 5) and the ‘San Lorenzo’ fault (g in Fig. 4 and F6 in Fig. 5) are two lineaments sub-parallel to the Passo della Morte fault. These three tectonic structures are very close to each other and are in proximity to the front of the anticline fold, thus determining the subdivision of the rock mass in several small-sized tectonic units.

## 4 Field Evidence

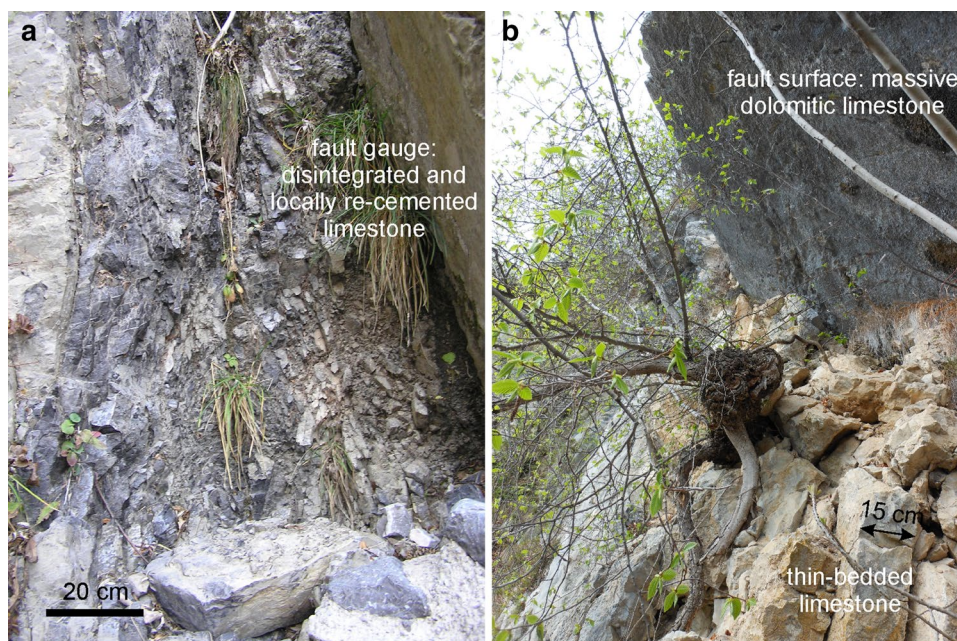
### 4.1 Block Assemblage and Major Discontinuities

The investigated rock mass is crossed by a number of major discontinuities (local faults) that subdivide the whole limestone spur into many secondary blocks with different structural conditions. These local faults are generally characterized by high continuity (length 10–100 m), low waviness and extremely low roughness (Fig. 7a, b). The fault surfaces are often smooth and frequent *striae* have been detected, testifying to relative motions between the adjacent blocks (Fig. 7c, d). Variable fault slips (10–70 cm) have been recognized. The fault surfaces show a highly variable degree of weathering, as also emphasized by some yellow-colored surfaces. The local faults are mainly characterized by rock-to-rock contacts, but some filling made up of crushed rocks has also been identified locally.

In the lower-eastern part of the limestone spur a set of sub-parallel faults (270/40) has been identified. One of these faults is characterized by numerous *striae* with plunge of 210–220° and inclination of 25°–30° (fault F7; Fig. 7b, d). In the western part of the limestone spur several faults with different orientation have been identified, clearly separating a number of sub-blocks forming the Western Spur (Fig. 8). There are four secondary blocks made up of thinly stratified limestone (BLOCKS 1–4) that are separated from the rear dolomitic rock mass (DOLOMITI BLOCK) by the Scluses Stream fault (F8 in Fig. 8b).

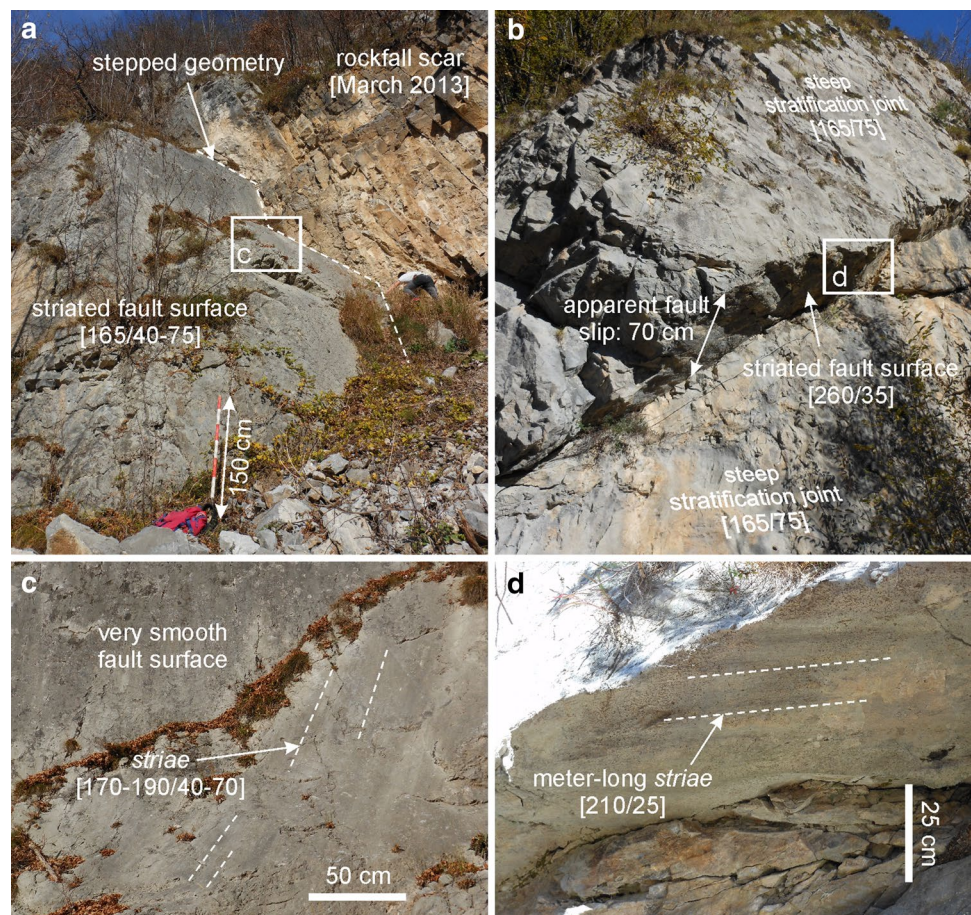
The largest and most persistent discontinuity identified on the field is the local fault outcropping at the failure scar

**Fig. 6** Details of the **a** Scluses Stream fault and **b** Passo della Morte fault. For the outcrop locations see Fig. 3





**Fig. 7** Local faults crossing the rock mass in the **a** western portion and **b** eastern portion of the limestone spur. For the outcrop locations see Fig. 3. **c, d** Details of the *striae* detected on the fault surfaces



of the March 2013 rockfall (Fig. 7a and F4 in Fig. 8b). This fault has a stepped geometry with a rather constant dip direction but a highly variable inclination (165/40–75). The fault surface is quite smooth with *striae* plunging in the same direction as the fault plane (Fig. 7c). In its upslope part, this major discontinuity has a lower dip (40°) and intercepts the Scuses Stream fault. Fault F4 locally bounds an upper, large rock block at the base (BLOCK1) that extends up to the spur culmination (Fig. 5). The limestone layers belonging to BLOCK1 are moderately fractured and locally folded. Occasional marly interbeds were also identified. The rock joints are sometimes open and filled by loose soil transported by water flow within the rock mass.

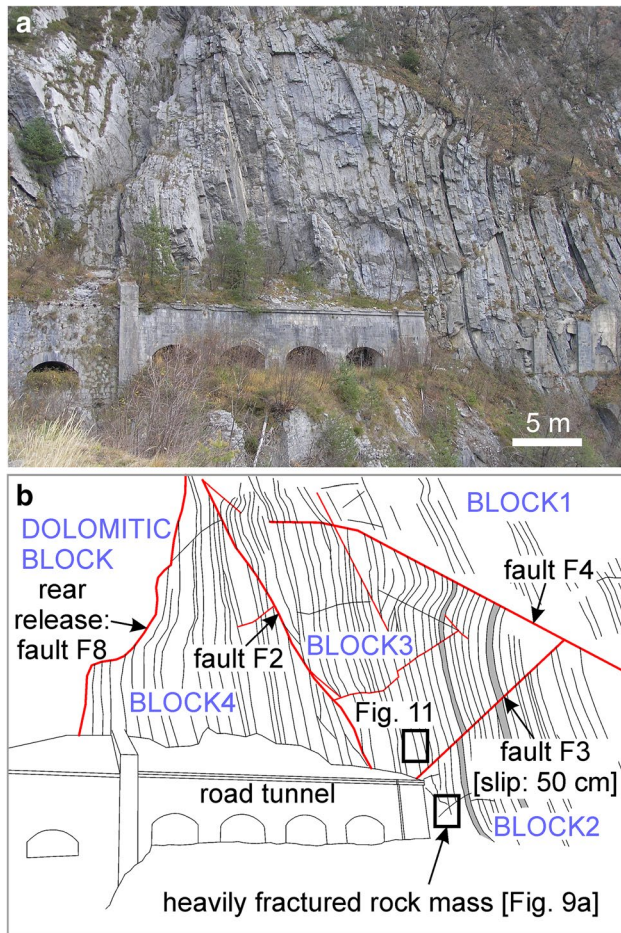
Fault F3 (340/35) is a cross-dip slope discontinuity with an apparent fault slip of 50 cm (dextral movement) that separates two blocks with very different rock mass damage (Fig. 8). The lower block at the toe of the slope (BLOCK2) is affected by a strong rock mass damage. This is the sub-block with the worst structural conditions. Fracturing is locally very high, with closely spaced and open joints that isolate very small blocks (even rotated) and that are sometimes filled with loose soil material (Fig. 9a). The rock layers are sometimes displaced and the joint surfaces are often weathered (Fig. 9b). Some folds with a large radius and

sub-vertical limbs have been recognized (Fig. 8). The adjacent sub-block (BLOCK3) has moderate rock mass damage, but fracturing increases from upslope downward (Fig. 8). The opening of the joints, the number and thickness of the marly interbeds (gray in Fig. 8b) increase towards the lower adjacent BLOCK2. At the top of BLOCK3, the rock layers are arranged so as to form a kink fold with a small radius (lower than 1 m, on average), thus demonstrating a remarkable deformation of the rock mass.

Fault F2 (180/60) is the lowermost major discontinuity crossing the investigated slope (Fig. 8). This fault intercepts upward the rear fault F8 but terminates downward in correspondence to the lowermost sub-block (BLOCK2), without daylighting at the toe of the slope. The fault surface is planar, continuous and rather smooth. This not-persistent discontinuity delimits an underlying rock block (BLOCK4) that is characterized by scarce rock mass damage, with undeformed rock layers and closed unfilled joints.

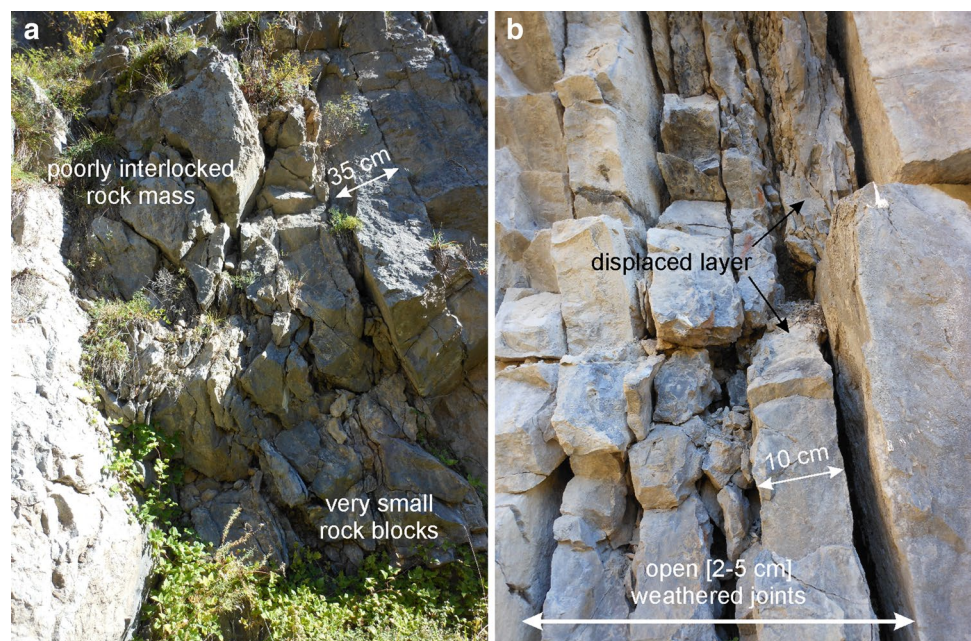
## 4.2 Rock Discontinuity Sets

A large amount of orientation data of both stratification and fracture joints has been acquired by means of the field survey ( $N=1108$ ; Fig. 10a), thus helping to define the structural



**Fig. 8** **a** The western scarp of the limestone spur and **b** its schematization showing the major discontinuities that cross the rock mass subdividing it into sub-blocks

**Fig. 9** Details of the rock mass structure at **a** the intersection of faults F2 and F3 and **b** the toe of the slope. For the outcrop locations see Fig. 3

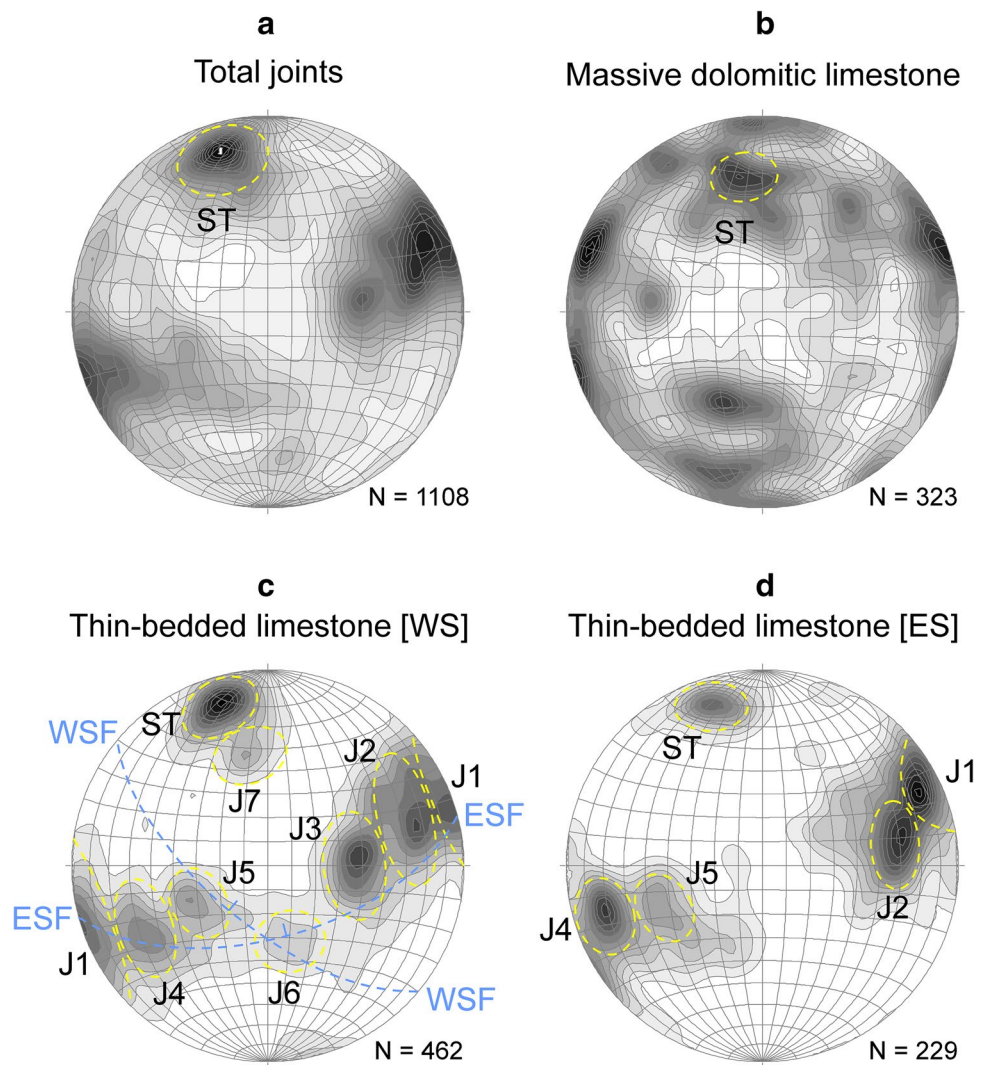


arrangements of the rock masses. For geomechanical purposes, three main structural units have been differentiated: (1) the rock mass made up of massive dolomitic limestone outcropping in the surroundings of the Western Spur (Fig. 10b); (2) the Western Spur formed by thinly stratified limestone (Fig. 10c); and (3) the Eastern Spur also made up of thinly stratified limestone (Fig. 10d).

Over the whole study area, the attitude of the stratification joints is very constant, only with a slight difference in their average dip. The limestone layers of both the Western Spur and the Eastern Spur have the same average orientation (Fig. 10c, d; Table 2); whereas the stratification joints of the massive dolomitic limestone have a lower mean inclination (Fig. 10b). This difference is consistent with the general structural arrangement of the rock mass forming the anticline fold affecting the north valley side (Fig. 5). In the stereographic projection of Fig. 10c, the great circles related to the western slope face (WSF 220/65) and to the eastern slope face (ESF 165/60) are also shown. When compared to the attitude of the more extended western slope face, the high-tilted stratification has a cross-dip slope orientation.

Several differences occur in both the number and the average orientation of the fracture joint sets identified in the three structural units (Fig. 10). Despite the larger number of measurements, the Western Spur (Fig. 10c) is characterized by a lower variability in the discontinuities orientation when compared with the rock mass made up of massive dolomitic limestone (Fig. 10b). This fact indicates that the fracturing pattern of the limestone spur is strictly related to a local stress field characterized by low variability over time. As a consequence, random fractures are limited. Seven main joint sets have been identified within the rock mass forming

**Fig. 10** Contoured pole plot (equal area projection) of stratification and fracture joints measured: **a** in the overall study area; **b** within the massive dolomitic limestone; **c** within the Western Spur; and **d** within the Eastern Spur



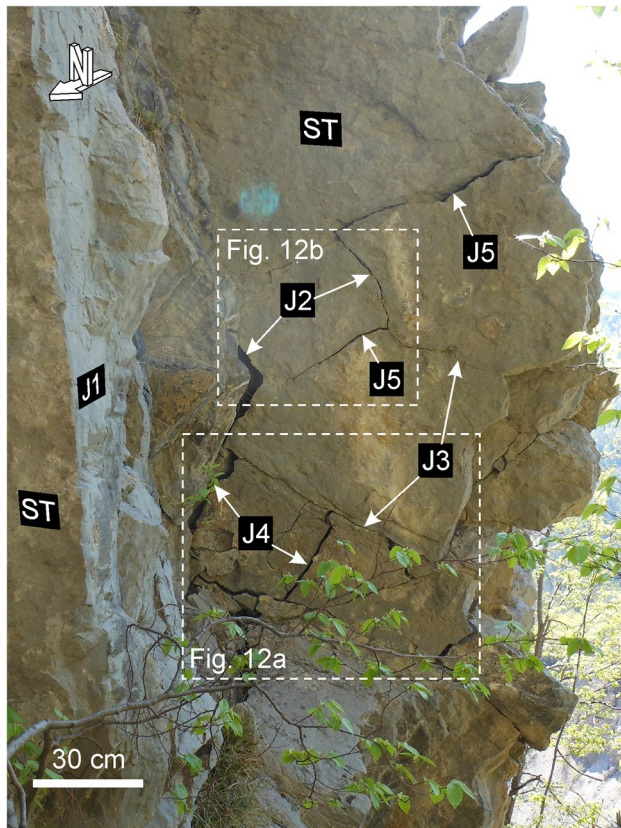
**Table 2** Joint orientation data from the Western Spur

Joint set	Joint type	No.	Dip dir. (N°E)	
			Mean ± St. dev.	Mean ± St. dev.
ST	Stratification	48	164 ± 07	74 ± 08
J1	Fracture	72	250 ± 14	85 ± 04
J2	Fracture	80	251 ± 16	66 ± 07
J3	Fracture	70	269 ± 17	40 ± 08
J4	Fracture	53	061 ± 13	63 ± 07
J5	Fracture	42	052 ± 22	36 ± 08
J6	Fracture	29	337 ± 15	38 ± 14
J7	Fracture	45	167 ± 12	63 ± 16

the Western Spur (J1–J7 in Fig. 10c; Table 2). Fractures belonging to sets J1–J5 have a dip direction sub-orthogonal to the bedding planes (Fig. 11). Joint sets J6 and J7 include fractures with a dip direction that is opposite and coincident, respectively, to the attitude of the stratification joints. Each

of the major discontinuities crossing the rock mass can be related to one specific joint set among the seven identified (Table 2). Faults F2 and F4 belong to set J7, which is characterized by variable inclination, whereas fault F3 can be related to set J6. The local faults detected in the lower-eastern part of the limestone spur (Fig. 7b) are mainly related to set J3; whereas the major discontinuities belonging to sets J6 and J7 were mainly detected in the western part of the limestone spur (Fig. 8).

The fracture orientation data from the Western Spur can be compared to the fracturing pattern that characterizes the Eastern Spur (Fig. 10d) since the two limestone slopes have the same orientation of bedding planes. On the whole, the two joint distributions are quite similar, as there are clear correspondences in the average orientation and relative frequency of some identified joint sets. Fracture orientation data from the Eastern Spur is generally characterized by low variability and four main joint sets have been identified (J1, J2, J4 and J5 in Fig. 10d). These joint sets have average



**Fig. 11** Outcrop showing the arrangement of the stratification joints and of the fracture joint sets sub-orthogonal to bedding. For the outcrop location see Fig. 8

orientations very close to the homologous sets detected in the Western Spur (Fig. 10c). Interestingly, there is a scarcity or absence of fractures belonging to sets J3, J6 and J7 previously recognized in the Western Spur.

### 4.3 Tectonic vs. Gravity-induced Joints

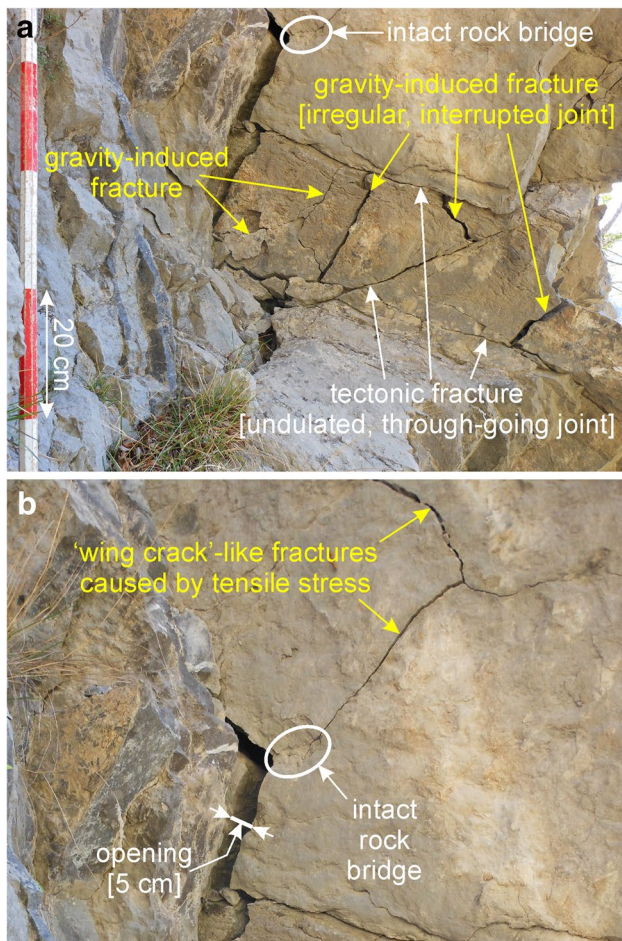
On the field, rock joints affecting the Western Spur highlight extremely variable properties in terms of persistence, waviness, spacing, opening, weathering and filling. Owing

to the low thickness of the limestone layers as well as to the high persistence of the bedding planes ( $> 10$  m), the rock slabs are subdivided by the cross-cutting joints into prismatic blocks of highly variable sizes (Fig. 11). The volume of the individual rock blocks ranges from 10 to 100 cm<sup>3</sup> (smaller compact blocks) up to 0.1–1 m<sup>3</sup> (larger flat blocks), depending on the fracture intensity. The number and spacing of fractures are highly variable on the investigated slope. In the innermost parts of BLOCK3 and BLOCK4, the joint spacing ranges from about 20–30 cm to 100–200 cm, depending on the specific joint set. These values of joint spacing are classified as ‘moderate’ and ‘wide’ according to the classification proposed by ISRM (1978). On the contrary, rock joints are more numerous and closely spaced within the rock masses localized in the intersection zones of the major discontinuities (Figs. 9a, 11) and at the toe of the slope (Fig. 9b). In these zones, the spacing between adjacent discontinuities belonging to the identified sets ranges from 5–10 cm to 10–20 cm, that are classified as ‘very close’ and ‘close’ (ISRM 1978).

The analysis of some rock outcrops localized in zones of the slope affected by higher fracturing allowed us to identify newly formed, gravity-induced fractures and differentiate them from joints of tectonic origin (Table 3). Figure 11 shows an outcrop located on the western scarp of the limestone spur, in correspondence with the intersection between faults F2 and F3 (Fig. 8). The rock mass is crossed by joints belonging to the identified fracture sets (Fig. 10c), but they highlight different characteristics in terms of persistence and geometry (Figs. 11, 12). Fractures of tectonic origin appear on the field as mainly undulated or locally planar (Fig. 12a). Their average heights of the asperities  $a$  are small ( $a = 1–10$  cm) if compared with the overall joint length  $l$  ( $l = 1–10$  m), that is with a ratio  $a/l$  of about 1–10%. These joints have ‘low’ to ‘medium’ persistence according to the classification proposed by ISRM (1978), and their profile is quite regular over their length, on average. Tectonic fractures are through-going joints that can intersect each other with highly variable values of the included angle of intersection, that ranges from 90° up to very small angles (10°–30°).

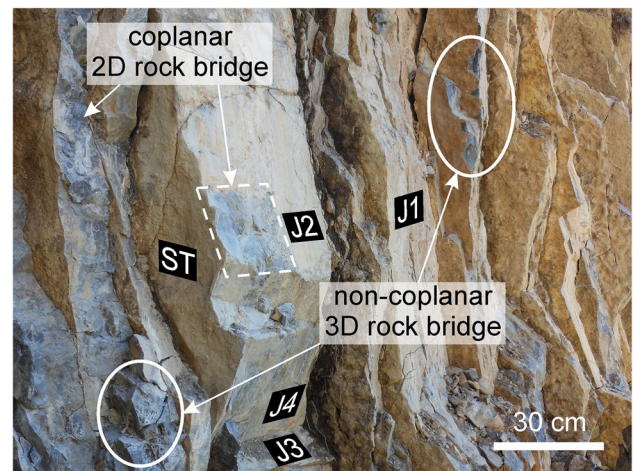
**Table 3** Geometrical characteristics of tectonic vs. gravity-induced joints identified on the field

Type of fracture	Geometry	Profile	Height of asperities/joint length ratio	Persistence	Included angle of intersection	In-situ placement
Tectonic	Undulated, locally planar	Mainly regular	0.1–1%	Through-going, ‘low’ to ‘medium’ (ISRM 1978)	Highly variable (10°–90°)	Widespread, ubiquitous
Gravity-induced	Jagged, abrupt changes in the main direction	Irregular and rough	1–20%	Interrupted, ‘very low’ (ISRM 1978)	Middle-to-high (50°–90°)	Toe of the slope, intersection of major discontinuities



**Fig. 12** **a** Geometrical characteristics of tectonic vs. gravity-induced joints recognized on the field. **b** Gravity-induced fractures caused by tension showing a typical ‘wing crack’ geometry. For the location of the pictures see Fig. 11

On the other hand, several fractures with different properties to those of tectonic joints have been recognized (Table 3). These fractures have irregular profiles with abrupt changes in their main direction, frequently showing a jagged geometry and consequently rougher surfaces (Fig. 12a). The height of the asperities ( $a = 1\text{--}5\text{ cm}$ ) is not small compared to the joint length ( $l = 5\text{--}30\text{ cm}$ ), with ratios  $a/l$  of about 1–20%. The latter is an order of magnitude higher compared to fractures of tectonic origin (Table 3). These joints have ‘very low’ persistence (ISRM 1978) and they frequently terminate against the through-going joints (Fig. 12a), intercepting them sub-orthogonally or with middle-to-high intersection angles ( $50^\circ\text{--}80^\circ$ ). Most of these joints are open, demonstrating that they were caused by tensile stress (Fig. 12a). Some tension-induced fractures identified on the field have variable opening over their length. They also curve towards a main constant direction (plumose structure) until coalescing with other joints or stopping at some finite crack length



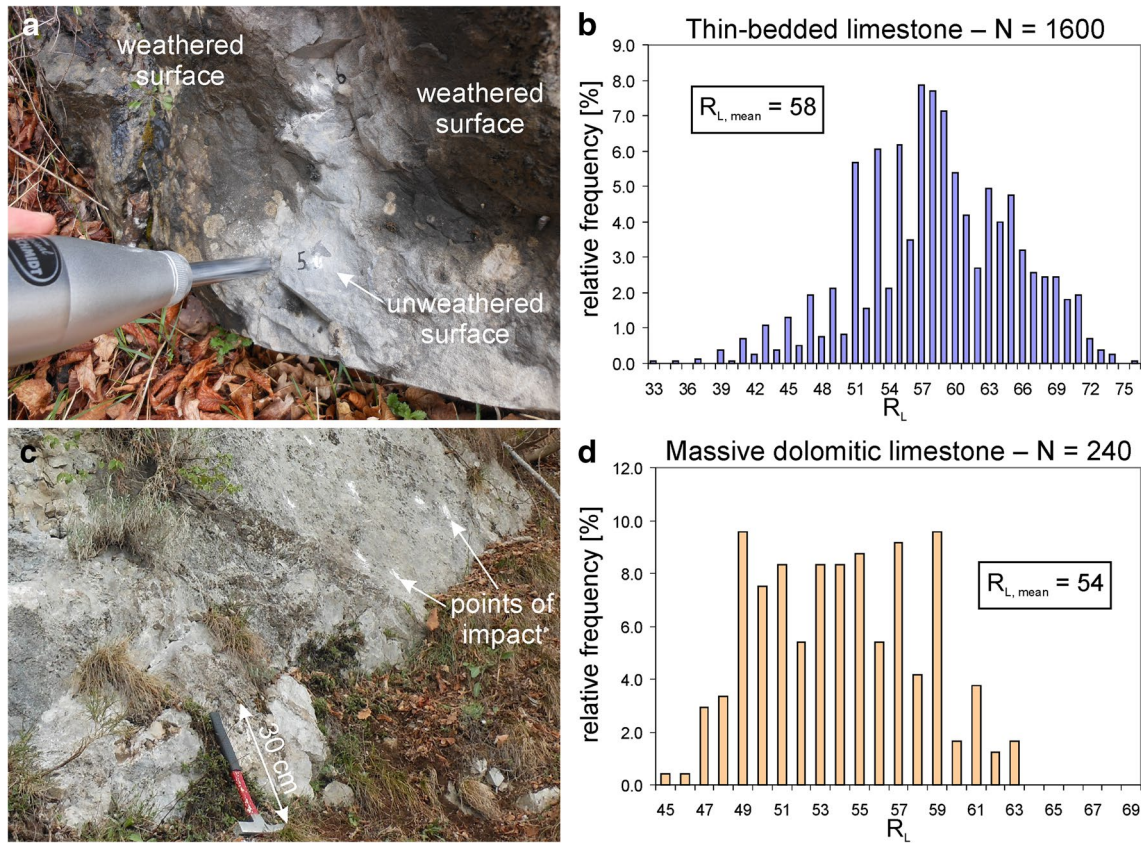
**Fig. 13** Field evidence of fracturing of coplanar and non-coplanar rock bridges in highly weathered rock mass (failure scar of shallow rockfall of March 2013)

against intact rock bridges (Fig. 12b). These joints have very similar geometry to wing cracks that are observed in laboratory tests which explore the failure mechanism of intact rock at the microscale (Horii and Nemat-Nasser 1985; Einstein and Dershowitz 1990; Park and Bobet 2009; Euser et al. 2019).

Fractures with the abovementioned characteristics represent gravity-induced joints caused by the local stress field acting at the slope scale. These newly formed joints are caused by tensile and shear stresses and are added to the pre-existing joints of tectonic origin as a result of the localized rupture of intact rock and rock bridges. The orientation and the spatial distribution of the newly formed fractures are strictly related to the 3D geometry of the rock masses and to the pre-existing joints (both stratification and tectonic joints). In some cases, fractures caused by gravity have the same orientation of the pre-existing joints, especially when they are the result of the rupture of coplanar (Tuckey and Stead 2016) or in-plane rock bridges (Fig. 13). In other circumstances, gravity-driven fractures show a different attitude compared to the pre-existing joints, being related to the rupture of non-coplanar (out-of-plane) rock bridges (Fig. 13).

#### 4.4 Intact Rock and Fault Surfaces Characterization

The uniaxial compressive strength (UCS) and the Young’s modulus ( $E$ ) of the intact rock have been estimated on the basis of some Schmidt hammer tests (type L) carried out at specific outcrops on the thin-bedded limestone (Fig. 14a, b) as well as on the massive dolomitic limestone (Fig. 14c, d). The measured rebound index values have been normalized according to Basu and Aydin (2004). The tests on the



**Fig. 14** Schmidt Hammer tests (type L) and related frequency histogram of the Rebound index measured on **a, b** thin-bedded limestone and **c, d** massive dolomitic limestone

thin-stratified limestone ( $N = 1600$ ) were performed on four different outcrops and both orthogonally and in parallel to the stratification joints, without, however, noting any significant difference. The overall trend of the rebound indexes obtained with the type L hammer shows a slightly asymmetric Gaussian distribution (Fig. 14b). The Schmidt hammer tests on the massive dolomitic limestone ( $N = 240$ ) were carried out on a single outcrop located on the failure scar to the east of the Western Spur. The overall trend of the rebound indexes obtained with the type L hammer shows a bimodal distribution (Fig. 14d).

The values of UCS and  $E$  for the intact rock have been calculated through empirical equations available in literature (Katz et al. 2000; Kahraman et al. 2002; Aydin and Basu 2005; Fener et al. 2005; Buyuksagis and Goktan 2007; Nazir et al. 2013). Remarkably, no suggestion exists in the literature for the determination of the reference value of the rebound index obtained from field tests and related to intact rock. Therefore, we defined realistic ranges of UCS and  $E$  by adopting various empirical equations and assuming different reference values of the rebound index: mean, mode, 75th percentile, 90th percentile, and maximum of the respective distributions. The identified ranges

are consistent with typical values of UCS and  $E$  related to the two rock types investigated (Hoek 2007). For the thinly stratified limestone, the value of the uniaxial compressive strength is included in the range  $UCS = 100\text{--}130$  MPa; whereas the value of the Young's modulus varies in the range  $E = 20\text{--}40$  GPa. For the massive dolomitic limestone, the value of the uniaxial compressive strength is included in the range  $UCS = 80\text{--}110$  MPa; whereas the value of the Young's modulus varies in the range  $E = 20\text{--}30$  GPa.

Some of the major discontinuities crossing the rock mass have been characterized according to the Barton–Bandis shear strength criterion (Table 4). Some Schmidt hammer tests were carried out to evaluate the joint compressive strength (JCS) of some fault surfaces. These tests were performed according to the suggested methods provided by ISRM (1978). The JCS values have been calculated by means of the empirical equations provided by Aydin and Basu (2005). On the whole, the joint compressive strength values of the fault surfaces vary in the range  $JCS = 40\text{--}90$  MPa (Table 4). This quite broad range testifies to the highly variable degree of weathering of the fault surfaces, as also ascertained during the field investigations.

**Table 4** Geomechanical parameters of some major discontinuities crossing the unstable rock mass, according to the Barton–Bandis shear strength criterion

Fault	Length $L_n$ (m)	Joint compressive strength JCS (MPa)	Joint roughness coefficient (uncorrected) $JRC_0$	Joint roughness coefficient (corrected) $JRC_n$	Residual friction angle $\varphi_r$ (°)	Peak friction angle $\varphi_p$ (°)
F1 (Fig. 6b)	100	46	20	1	26.6	30.9
F2 (Fig. 8)	25	40	20	2	24.2	25.6
F3 (Fig. 8)	10	93	20	3	27.9	34.6
F4 (Fig. 7a, c)	50	75	20	2	27.0	30.1
F7 (Fig. 7b, d)	20	49	20	2	25.2	27.5

Some roughness measurements were also carried out to determine the joint roughness coefficient (JRC) of the fault surfaces. The amplitude of asperities of the joint surfaces were measured with a reference straight edge having a length of 100 mm, to determine the joint roughness related to the standard size of the rock joints usually tested in the laboratory ( $JRC_0$ ). The values of  $JRC_0$  have been determined by means of the roughness chart provided by Barton and Bandis (1990). The scale effect has been accounted for considering the actual length of the fault surfaces ( $L_n = 10–100$  m). As expected, the values of the corrected joint roughness coefficient ( $JRC_n$ ) are extremely low, varying in the range  $JRC_n = 1–3$  (Table 4).

The residual friction angle ( $\varphi_r$ ) of the tested fault surfaces have been determined according to the empirical equation provided by Barton and Choubey (1977). When assuming a basic friction angle ( $\varphi_b$ ) equal to  $30^\circ$ , as suggested by Barton and Choubey (1977) for flat un-weathered joint surfaces of limestone rock, the residual friction angle of the fault surfaces analyzed is included in the range  $\varphi_r = 24^\circ–28^\circ$  (Table 4). The corresponding values of the peak friction angle ( $\varphi_p$ ) essentially vary between  $\varphi_p = 25^\circ$  and  $\varphi_p = 35^\circ$ . The Barton–Bandis field characterization highlighted that the fault surfaces crossing the rock mass have different shear strength properties. In particular, faults F2 and F7 are characterized by lower values

of the peak friction angle if compared with faults F4 and F3 (Table 4).

### 4.5 Rock Blocks Mechanical Parameters

The geomechanical parameters of the rock masses have been evaluated in relation to the various blocks that form the investigated slope (BLOCKS 1–4) as well as the rear rock mass (DOLOMITIC BLOCK). The strength parameters and the deformability of each rock block have been assessed by means of a rock mass field characterization based on the Hoek and Brown criterion (Hoek 2007). The mechanical parameters of the five blocks are listed in Table 5. The compressive and tensile strengths, the Young’s modulus, and the equivalent Mohr–Coulomb shear strength parameters of the rock masses have been calculated by means of empirical equations (Hoek 2007), on the basis of the mechanical characteristics of both the intact rock and the rock mass. The compressive strength ( $\sigma_{ci}$ ) and the Young’s modulus ( $E_i$ ) of the intact rock for the thin-stratified limestone as well as for the massive dolomitic limestone correspond to the respective average values of the ranges of UCS and E previously evaluated through the Schmidt hammer tests (see Sect. 4.4). The intact rock constant ( $m_i$ ) essentially depends on the lithological features of the specific geological formation. Its value has been determined by means of the rock property database

**Table 5** Geomechanical parameters of the identified rock masses, according to the Hoek and Brown field characterization

Rock mass	Uniaxial compressive strength of intact rock $\sigma_{ci,mean}$ (MPa)	Young’s modulus of intact rock $E_{i,mean}$ (MPa)	Constant for intact rock $m_i$	Geological Strength Index GSI <sub>mean</sub>	Rock mass compressive strength $\sigma_c$ (MPa)	Rock mass tensile strength $\sigma_t$ (MPa)	Cohesion $c$ (MPa)	Friction angle $\varphi$ (°)	Young’s modulus $E_{rm}^a$ (MPa)
BLOCK1	115	30,000	8	35	2.77	-0.11	0.51	52	3402
BLOCK2	115	30,000	8	30	1.98	-0.07	0.39	51	2441
BLOCK3	115	30,000	8	40	3.80	-0.16	0.66	52	4790
BLOCK4	115	30,000	8	45	5.15	-0.23	0.82	53	6709
DOLOMITIC BLOCK	95	25,000	9	50	5.72	-0.24	0.93	53	7680

<sup>a</sup>Hoek and Diederichs generalized equation (Hoek and Diederichs 2006)

available in the code RocData (Rocscience 2007). According to these values, the intact rock constant is  $m_i = 8$  for the thin-bedded limestone and  $m_i = 9$  for the massive dolomitic limestone (Table 5).

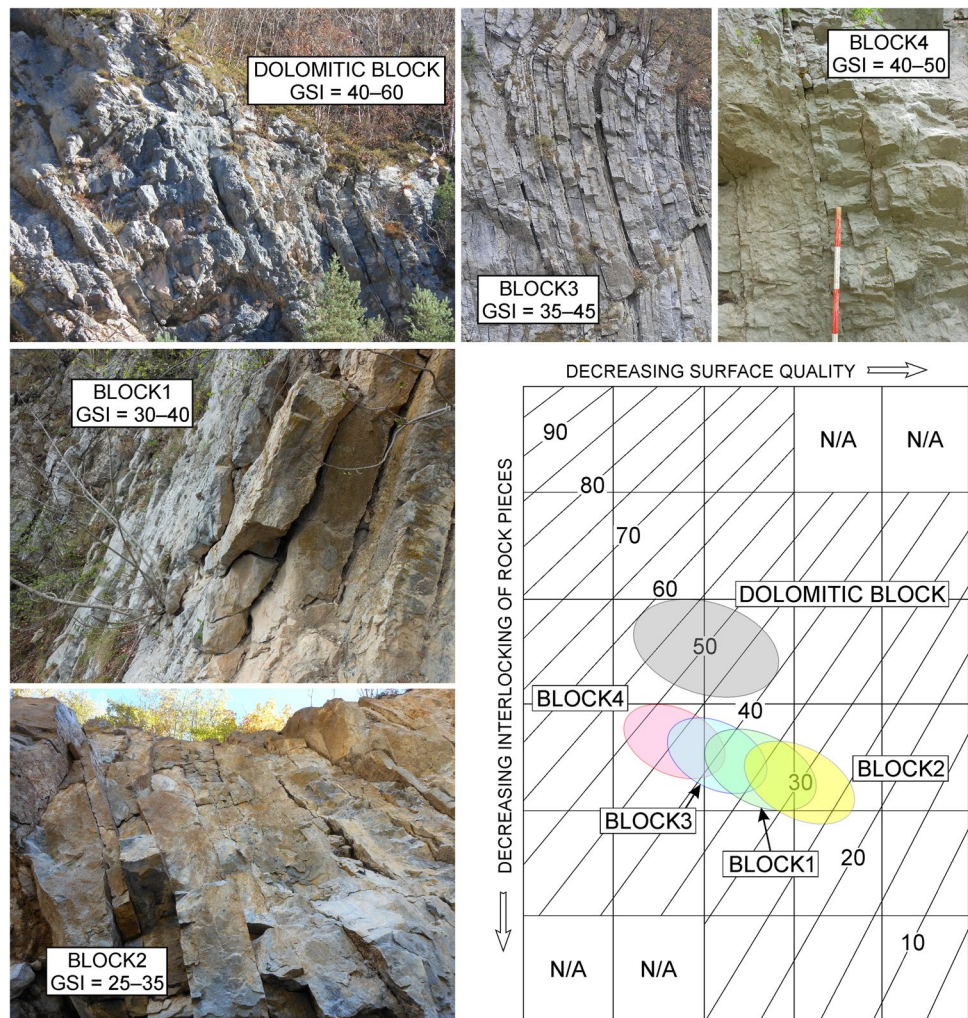
For each rock block, a proper range of the Geological Strength Index (GSI) has been determined on the basis of the field evidence (Fig. 15; Table 5). The condition of the different rock masses differs in the degree of fracturing and in the surface condition of the discontinuities. The rock block made up of massive dolomitic limestone (DOLOMITIC BLOCK) has a ‘very blocky’ structure owing to the presence of at least four joint sets (Fig. 10b). The joint surface condition varies between ‘good’ and ‘fair’ since the discontinuities are generally rough with moderate weathering and without any filling. The range of GSI related to DOLOMITIC BLOCK (GSI=40–60) is the highest among the identified rock masses (Fig. 15; Table 5).

The rock blocks made up of thin-stratified limestone (BLOCKS 1–4) have a ‘blocky-disturbed-seamy’ structure owing to the persistence of the bedding planes and to the

presence of many intersecting joint sets (Fig. 10c). The GSI values of the limestone blocks essentially vary on the basis of the degree of weathering of the joint surfaces as well as on the presence of marly interbeds or soil fillings (Fig. 15; Table 5). When considering field observations (see Sect. 4.1), the surface quality of the discontinuities varies, on the whole, from ‘good’ (BLOCK4) to ‘poor’ (BLOCK2). As a result, the GSI values related to the limestone blocks are rather variable (Fig. 15; Table 5), gradually increasing from the lowest values related to BLOCK2 (GSI=25–35) up to the highest values for BLOCK4 (GSI=40–50). The notable variability in the GSI values of the rock masses emphasizes the structural heterogeneity of the adjacent rock blocks that was recognized on the field.

The compressive strength of the rock masses essentially varies between 2 MPa and 6 MPa; whereas the tensile strength is much lower, in the order of about 100–200 kPa (Table 5). The equivalent Mohr–Coulomb shear strength parameters (cohesion  $c$  and friction angle  $\varphi$ ) of the five-rock blocks have been estimated through the linearization of the

**Fig. 15** Geological Strength Index GSI of the various rock blocks potentially involved in the failure of the Passo della Morte slope, according to the Hoek–Brown criterion (Hoek 2007)





respective curvilinear Hoek–Brown failure envelopes. For this linearization procedure, the value of the upper limit of the confining stress ( $\sigma'_{3max}$ ) has been determined by accounting for the slope height of each block ( $H = 50\text{--}100\text{ m}$ ), as suggested by Hoek (2007). The equivalent friction angle values of the five blocks are quite similar and higher than  $\varphi = 50^\circ$  (Table 5); whereas the equivalent cohesion varies from a minimum value equal to about  $c = 400\text{ kPa}$  (BLOCK2) up to a maximum value of about  $c = 900\text{ kPa}$  (DOLOMITIC BLOCK). Finally, the Young's modulus of the blocks, calculated by means of the Hoek and Diederichs generalized equation (Hoek and Diederichs 2006) varies between a minimum value of about 2.4 GPa for BLOCK2 and a maximum value of about 7.7 GPa for DOLOMITIC BLOCK (Table 5).

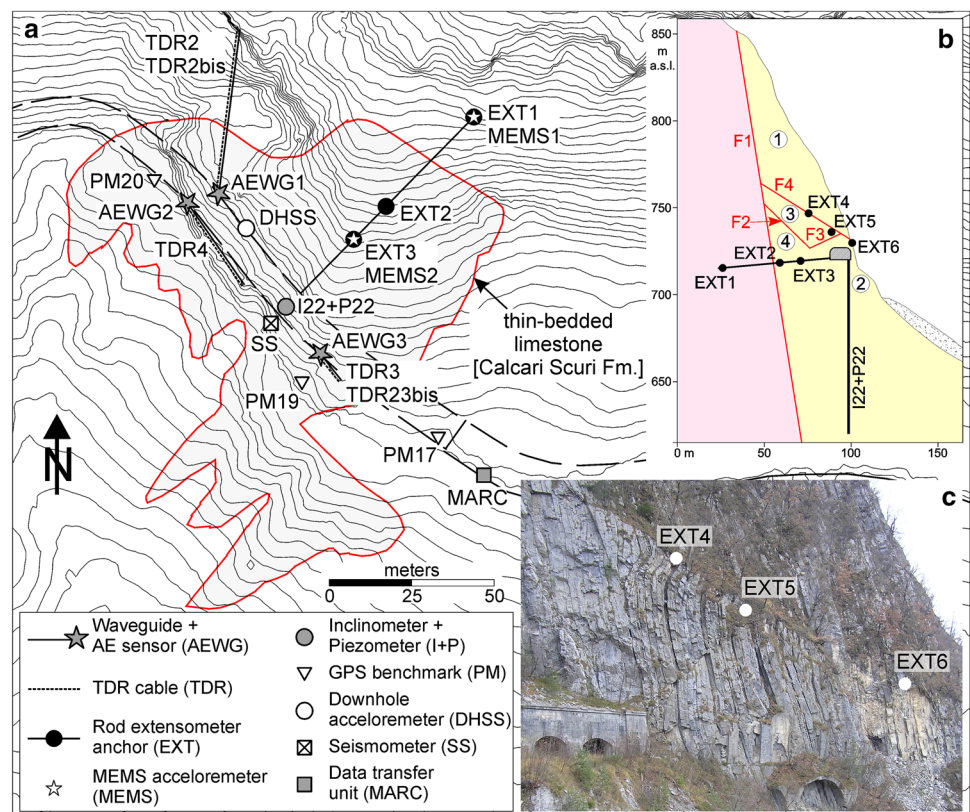
### 4.6 Slope Monitoring Data

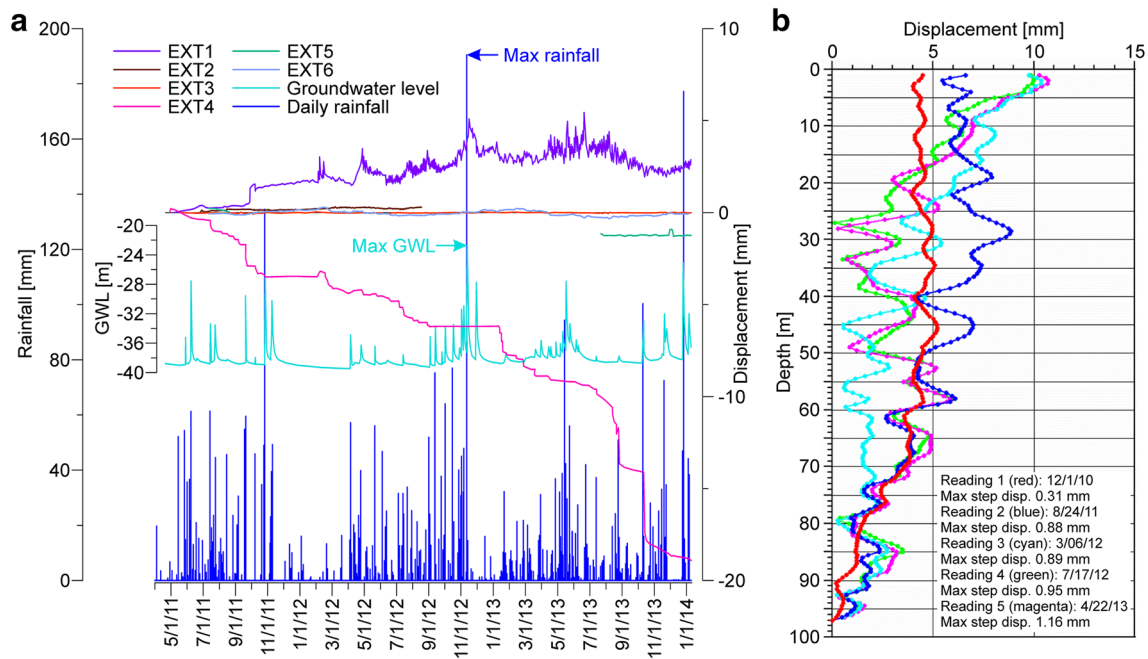
The monitoring system installed on the Western Spur by the IRPI-CNR includes (Fig. 16): three Acoustic Emission (AE) sensors, five Time Domain Reflectometry (TDR) cables, a three-point rod extensometer, an inclinometer, a piezometric sensor, three accelerometers, a seismometer, three extensometers and three GPS benchmarks. In addition, Terrestrial Laser Scanning (TLS) and Infra-Red Thermography (IRT) surveys were carried out to identify critical joints and weak zones of the rock mass (Teza et al. 2015).

Three extensometers (EXT1, EXT2 and EXT3) were installed in a sub-horizontal borehole drilled through the limestone slope from within the road tunnel (Fig. 16a, b). According to the data provided by the Civil Protection of the Friuli Venezia Giulia Region (Marcato et al. 2014), extensometers EXT2 and EXT3 did not measure significant displacements in the period May 2011–January 2014; whereas extensometer EXT1 registered sub-centimeter movements (Fig. 17a). The displacement pattern points out an alternation of widening and shortening that is believed to be caused by differential movements among distinct internal blocks (Marcato et al. 2014). There is no clear correlation between the displacements registered by extensometer EXT1 and the rainfall data (Fig. 17a).

Three additional extensometers (EXT4, EXT5 and EXT6) were installed on the western scarp of the limestone spur (Fig. 16c). Extensometer EXT4 was placed across a bedding plane that intersects fault F4 in correspondence to the kink fold at the contact between BLOCK1 and BLOCK3; whereas extensometers EXT5 and EXT6 were placed across two bedding planes within, respectively, BLOCK3 and BLOCK2, the latter just above the failure scar of the shallow rockfall of March 2013. Extensometer EXT4 registered a cumulative displacement of about 20 mm in the period May 2011–January 2014 (Fig. 17a). The displacement pattern is stepped, with impulsive movements along the discontinuity. On the

**Fig. 16** **a** Schematic plan of the monitoring system installed by the IRPI-CNR on the Passo della Morte slope (modified from Codeglia et al. 2017). **b** Projection on the cross-section B–B'' of the extensometers, inclinometer and piezometer. **c** Location of extensometers EXT4–6 installed on the western scarp of the limestone spur





**Fig. 17** **a** Displacement patterns and groundwater levels measured by the extensometers and piezometer P22 installed on the Passo della Morte slope. **b** Deep displacements registered by inclinometer I22.

Data provided by the Civil Protection of Friuli Venezia Giulia Region (Marcato et al. 2014)

contrary, extensometers EXT5 and EXT6 did not measure any significant deformation (Fig. 17a), i.e. the measurements were below the instrument accuracy threshold (Teza et al. 2015).

Three GPS benchmarks (PM17, PM19 and PM20) were installed on the slope face at the elevation of the abandoned national road (Fig. 16a). No displacements were measured by benchmarks PM17 and PM19; whereas benchmark P20 registered a counter-slope down movement of 3.5 cm. However, this benchmark was installed on an overhanging rock block and probably registered a back tilting movement that is not representative of the overall rock mass deformation (Marcato et al. 2014). No information is available about the deformations registered by the TDR cables.

An inclinometer (I22) and a piezometric sensor (P22) were placed in a 100-meter-long vertical borehole drilled from the road tunnel (elevation: 720 m a.s.l.; Fig. 16a, b). The deformation pattern highlighted by the inclinometer data, which is characterized by sub-centimeter displacements, did not reveal any sliding surface (Fig. 17b). The piezometric sensor measured the groundwater level variations continuously over the period of monitoring (Fig. 17a). A groundwater table ordinarily placed at  $-39$  m from the road level was identified. The groundwater level increases rapidly (in few hours) as a result of rainy periods, with subsequent discharges in the following 2–3 days. The highest groundwater level was reached in November 2012, with an increase up to about  $-23$  m from the road level (Fig. 17a).

Finally, Acoustic Emission (AE) events were registered by three sensors installed in sub-horizontal boreholes drilled in the frontal part of the slope, at the elevation of the road tunnel (Fig. 16a). The AE events were related to both groundwater pressure variations within the fractured rock mass and snow loading on the slope (Codeglia et al. 2017).

On the basis of the slope monitoring data previously reported, the following considerations can be made:

1. According to the displacements measured by extensometer EXT4, fault F4 is actually an internal sliding surface. The low-magnitude and stepped pattern of the movements are indicative of brittle behavior affecting the stiff rock slope.
2. The null displacements measured by extensometers EXT5 and EXT6 point out that no deformation takes place along the bedding planes.
3. The absence of a sliding surface revealed by inclinometer I22 demonstrates that the lowermost faults crossing the rock mass (faults F2 and F7) do not outcrop at the slope toe and that a potential rupture surface is still not formed.
4. As highlighted by its level variations measured by piezometer P22, the groundwater table remains low enough to avoid the occurrence of uplifting forces along the local faults representing possible sliding surfaces; and

5. The recording of AE events demonstrates the occurrence of localized failures of intact rock that effectively involve the rock mass.

## 5 The Engineering–Geological Model

On the basis of the geological and morphological context of the study area and considering all the field evidence previously described, we have established an engineering–geological model of the Passo della Morte slope. This geomechanical model takes into account the potentially unstable rock blocks susceptible to failure, along with their rupture surfaces, volumes and failure kinematics. A preliminary assessment of the slope stability condition has also been advanced.

### 5.1 Slope Progressive Failure

The identified fault slips and striated surfaces as well as the displacements registered by one extensometer (EXT4) are all kinematical clues that prove relative movements among the adjacent blocks forming the Western Spur. Owing to their persistence, smoothness and orientation, the local faults crossing the rock mass are possible basal sliding surfaces of unstable blocks susceptible to failure. The Western Spur is also characterized by highly persistent and low-spaced bedding planes as well as by a large number of fracture joint sets (J1–J7). Some of these joint sets (J3, J6 and J7 in Fig. 10c) were only detected within the Western Spur and are absent in a nearby limestone slope that is structurally similar and considered as stable (Eastern Spur). The abovementioned aspects represent important geomechanical evidence of strong fracturing and internal subdivision of the investigated rock mass.

The field survey ascertained that the fracture intensity is not homogeneous throughout the slope and rock jointing mainly concentrates at the toe of the slope (BLOCK2) as well as in the zones of intersection of the local faults and at their tips (Figs. 9, 11). The toe of the slope is a critical part of the limestone spur since it is characterized by a strong change in the slope inclination that induces stress concentration. Stress concentrations also arise in correspondence to the discontinuity tips and around stiff indented parts of rock mass where displacements are inhibited or constrained, such as at the intersection of discontinuities. These localized zones of stress concentration are responsible for crack initiation, propagation and coalescence. Field investigations show that rock masses located in zones of the slope affected by high-stress states (Figs. 9, 11, 12, 13) are characterized by a widespread presence of newly formed, gravity-induced fractures. This evidence demonstrates that the rock mass locally accumulated strong damage, favoring the progressive

development of new internal rupture surfaces and thus determining an overall strength decrease. Notably, the 2013 rock-fall occurred in the critical part at the toe of the slope.

All the aforementioned issues represent geomechanical evidence of a progressive failure phenomenon that involves the Passo della Morte slope. Field evidence testifies that the Western Spur has a stability condition very close to the limit equilibrium, i.e. approaching slope collapse. The overall mechanical behavior of the slope is mainly governed by the kinematic conditions of the secondary blocks, which in turn, depend on the geometry and mechanical properties of the major discontinuities that delimit the blocks. The stratification joints have little influence on the mechanical behavior of the limestone spur. This is explained by the following evidence: (1) the dip direction of bedding planes ( $164^\circ$ , on average) is oblique when compared to the potential sliding direction ( $205^\circ$ – $220^\circ$ ); (2) two extensometers installed across bedding planes (EXT5 and EXT6) did not register any relative movement; (3) the folding and related waviness affecting the thin-bedded limestone locally determines an increase in shear strength along and between the stratification joints, causing more interlocking of the rock layers and inhibiting dilation and kinematic movement. Higher driving forces are required to either override or shear through the folds.

Thus, despite their high tilting (dip angle:  $74^\circ$ , on average), the bedding planes remain mainly passive when related to the overall mechanical behavior of the slope. Nevertheless, the low thickness of the limestone layers favors the occurrence of newly formed cross-cutting joints in low-confinement over-stressed zones of the slope, possibly causing surface toppling and/or buckling failures of individual rock slabs. As a consequence, the secondary blocks behave as homogeneous distinct rock masses that interplay through delimiting discontinuities. The sub-blocks are also affected by internal damage caused by localized over-stress that varies over time and space as a function of internal slope displacements and intact rock fracturing. This particular mechanical behavior has to be kept in mind when choosing the proper calculation approach and numerical tool to analyze the stress–strain behavior of the slope.

### 5.2 Failure Scenarios

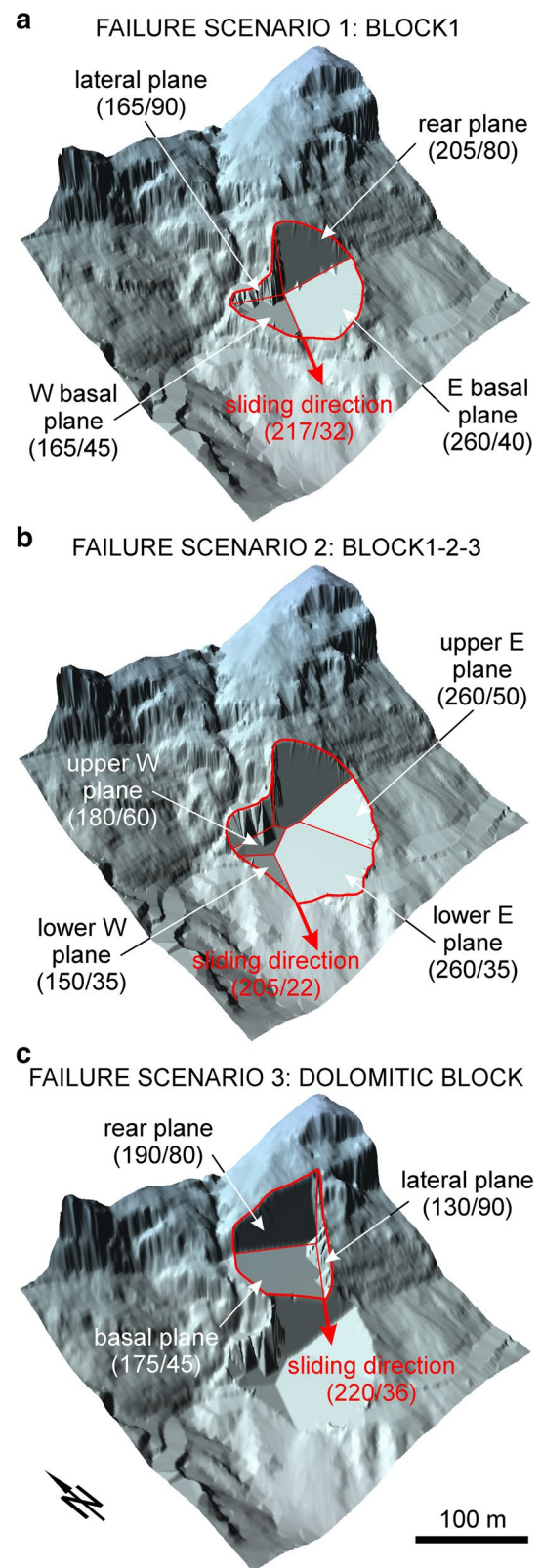
The field survey ascertained that the local faults with a dip direction towards the SSE (set J7 in Fig. 10c) prevail in the western part of the limestone spur, whereas in its eastern part the west-dipping faults (set J3 in Fig. 10c) are predominant. When considering the three-dimensional geometry of the slope, most of the identified rock blocks are partially or nearly completely bounded by some intersecting fault surfaces. On the basis of the orientation of the major discontinuities crossing the limestone spur as well as of the

structural condition of the recognized rock blocks, three different failure scenarios have been identified (Fig. 18). The rock volumes susceptible to failure have been estimated considering the specific planes that delimit the unstable blocks (basal planes as well as lateral and rear release surfaces) and the actual topographic surface, which was reconstructed by means of the DTM.

Failure scenario 1 is associated with the possible collapse of BLOCK1, which is the uppermost block forming the Western Spur (Fig. 18a). BLOCK1 is bounded at its base by two rather continuous planes. The western basal plane is fault F4 (165/45); whereas the eastern basal plane (260/40) belongs to the fault set characterizing the lower-eastern part of the limestone spur. These two basal planes form an intersection line (217/32) that daylights at the western slope face just above the failure scar of the rockfall which occurred in March 2013 (Figs. 5, 18a). The plunge of the intersection line of the two basal planes is very close to the dip direction of the western slope face (220°), thus determining a typical wedge-type failure kinematism. The Passo della Morte and Scuses Stream faults represent the rear/lateral detachment surfaces of BLOCK1. The calculated volume of this uppermost, unstable part of the Western Spur is about 110,000 m<sup>3</sup>.

Failure scenario 2 involves a larger and deeper portion of the Western Spur that is formed by the assemblage of BLOCK1, BLOCK2 and BLOCK3 (Fig. 18b). As for failure scenario 1, the Passo della Morte and Scuses Stream faults represent the rear/lateral releases of this unstable multi-block. The basal sliding surface has a complex, multi-planar geometry and is not fully formed. In fact, this unstable part of the limestone spur is bounded at its base by three local faults that do not outcrop at the slope face. On the western side, fault F2 (180/60) delimits the multi-block in its innermost part, whereas on the eastern side two basal planes have been identified: an upper one (260/50) and a lower one (fault F7: 260/35; Fig. 7b).

Both faults F2 and F7 terminate in correspondence to BLOCK2 at the toe of the slope, without, however, outcropping at the lower western slope face. This surface evidence is confirmed by the data obtained by the inclinometer that did not reveal the presence of a rupture surface at depth. As a result, the potential failure surface is not fully formed, and BLOCK2 represents a resisting part of rock mass at the toe of the slope. The formation of a new rupture surface within BLOCK2 is required to make the slope collapse possible. The volume of the multi-block involved in failure scenario 2 (BLOCK1-2-3) has been estimated by taking into account a completely formed 3D surface that considers two possible rupture planes in the outermost part of BLOCK2 (Fig. 18b). The unstable volume is about 200,000 m<sup>3</sup>. The complex geometry of the basal sliding surface determines a wedge-type failure kinematism. When considering the orientation of the pre-existing fault surfaces and of the newly formed



**Fig. 18** 3D rupture surfaces hypothesized within the unstable slope and associated with the collapse of **a** BLOCK1, **b** BLOCK1-2-3, and **c** DOLOMITIC BLOCK

rupture planes, the sliding direction is 205/22 (Fig. 18b), which is close to the dip direction of the western slope face.

Failure scenario 3 considers a retrogressive slope failure that involves a block made up of massive dolomitic limestone (DOLOMITIC BLOCK) resting behind the Western Spur (Fig. 18c). In fact, the possible collapse of the limestone spur would determine a sudden modification in the slope geometry. When considering the presence of continuous faults (F5 and F6 in Fig. 5) acting as possible rear releases, the loss of the buttressing effect provided by the Western Spur could cause a destabilization of a rear rock block. Owing to the morphology of the slope, the retrogressive slope failure could occur for both failure scenarios involving the limestone spur, i.e. for the collapse of the uppermost block (BLOCK1) as well as for the larger multi-block (BLOCK1-2-3).

Owing to the difficult operative field conditions, the three-dimensional geometry of DOLOMITIC BLOCK has been determined on the basis of the morphological features and the tectonic-structural arrangement of the rock scarps (Fig. 18c). This unstable block is bounded at its back by the San Lorenzo fault (190/80; F6 in Fig. 5); whereas the eastern lateral release (130/90) is represented by a master joint crossing the rock mass adjacent to the failure scar of the Clap di Lavres landslide (Fig. 4). A free slope face characterizes the western lateral margin towards the Scuses Stream. Although it was not possible to identify the basal sliding surface exactly, the latter has been assumed in order to maximize the possible volume of the retrogressive slope failure. Thus, the basal sliding surface is represented by a stratification joint that has the same orientation (175/45) as a bedding plane actually measured on the detachment surface close to the east of the Western Spur. The Caprera fault (F5 in Fig. 5) subdivides the whole unstable block into two adjacent sub-blocks. When considering the failure kinematism of DOLOMITIC BLOCK, the eastern limit represents a lateral constraint that would determine a strong asymmetric wedge-type failure. The possible sliding direction coincides with the intersection line between the basal plane and the lateral constraint (220/36, Fig. 18c). The volume of potential retrogressive failure has been estimated as equal to 135,000 m<sup>3</sup>.

On the whole, the worst failure scenario is associated with a two-stage retrogressive rupture that assumes an initial slope failure involving BLOCK1-2-3 followed by the collapse of DOLOMITIC BLOCK. In this case, the total estimated unstable volume amounts to 335,000 m<sup>3</sup>.

## 6 Discussion and Conclusions

The critical stability condition of the Passo della Morte slope can evolve, even in a short time, into slope collapse, thus determining a high landslide hazard. The slope failure

could occur as a consequence of a specific triggering factor (earthquake or intense/prolonged rainfall) or even as a result of a fatigue process related to the progressive failure that actually involves the Western Spur. The slope progressive failure is a preparatory mechanical process responsible for damage initiation and propagation up to slope collapse that can be triggered by both natural and human causes and has a highly variable duration (from hours or days to thousands of years). The larger the size of the involved rock slope, the longer the time required to generate the condition for collapse (Abele 1994). Excavation activity in underground or shallow mining as well as re-profiling of engineered slopes can trigger small-sized rock slope failures characterized by a very quick process of crack growing and coalescence, eventually leading to a sudden collapse of rock slabs or blocks. For high natural rock slopes, the progressive failure process is mainly influenced by the geomorphological events that have occurred in the last few thousand years in mountainous regions.

The progressive formation of a fully developed three-dimensional failure surface through the coalescence of pre-existing discontinuities and newly formed brittle fractures requires a very long time-span (from 1000–2000 years to 10,000–20,000 years). According to Prager et al. (2008), rock slope failures and large mass movements (volume > 10 million m<sup>3</sup>) in the Alps have occurred with a rather continuous temporal distribution since the end of the Last Glacial Maximum (LGM). The rapid glacial retreat which began at the end of the LGM (18,000–19,000 year BP) is the starting point of slope instability processes that were essentially promoted by the kinematic freedom acquired by the Alpine valley slopes (Prager et al. 2008; McColl 2012). However, the duration of the progressive failure phenomenon strictly depends on the interaction of local predisposing geological factors (mainly lithology and tectonic setting), seismic activity and climatically controlled groundwater flows. The concurrence of some unfavorable factors may accelerate the mechanical process of rock mass damage that leads to slope collapse: dip-slope attitude of bedding or planes of weakness (schistosity), thin stratification or multilayer sequences, presence of weak interbeds (clay/marl layers), presence of continuous delimiting faults, intense tectonic damage of the rock mass, occurrence of frequent and/or strong earthquakes and intense/prolonged rainfall. On the contrary, the absence of key predisposing factors results in a prolonged stable condition of the valley slopes.

The geomechanical study of the Passo della Morte slope explains how the rapid deglaciation of this Alpine valley and the subsequent valley floor deepening related to river erosion determined strong morphological modification of the valley slopes. The debuttressing effect caused by these climatic-controlled events, along with the presence of some tectonic structures affecting the valley slopes (such as the

Passo della Morte and Seluses Stream faults), caused a local stress field at the slope scale that was responsible for progressive fracturing of the rock mass. In addition, cycling loading related to the occurrence of strong earthquakes in this area, freeze–thaw and hydraulic over-pressures caused by intense or prolonged rainfalls, or even by hydrogeological anomalies, may have resulted in accumulation of rock mass damage.

When considering the current geomorphological setting of the Tagliamento River valley in the surroundings of the investigated slope, the possible collapse of the Western Spur would determine a severe risk situation. Owing to the potential sliding direction of the collapsed limestone spur, the rockslide mass would propagate towards the valley bottom, possibly resting on it and originating a landslide dam with a lake at its back. The possible subsequent collapse of the landslide dam (i.e. the dam break) would cause flooding that would pose a considerable threat to the villages and infrastructures located downstream. Thus, the investigated slope stability problem results in a typical cascading risk analysis.

The study carried out on the Passo della Morte slope emphasizes the importance of field investigations in detecting geomechanical evidence of rock mass damage affecting unstable rock slopes during the delicate phase that precedes the collapse. When facing a priori stability analyses, a geomechanical survey must be aimed at recognizing the presence of large discontinuities (possible internal sliding surfaces), kinematical clues of internal slope movements (fault slips, slickensides), zones of intense rock mass damage (closely spaced and open fractures, disintegrated rocks, brittle folds), as well as to collect very detailed data on rock joints and rock masses. Geomechanical evidence acquired from the field should be considered to design slope monitoring and laboratory tests properly. Sometimes, slope monitoring devices are planned and placed without a proper knowledge of the mechanical behavior of the rock mass provided by preliminary field observations. Mechanical indicators of rock mass damage recognized on the field represent useful data to choose the most appropriate location for sampling of rock materials for laboratory analyses and for in situ measurement of spatial and temporal variations in pore pressures, slope displacements, stresses and internal rock mass deformations. In this way, the combination of field observations and slope monitoring provides valuable data to understand the mechanisms driving the instability and to compare the results of numerical modeling with objective observations.

On the whole, the present paper shows that to study slope stability problems involving high natural rock slopes we must consider the interaction between pre-existing discontinuities, internal secondary blocks subdividing the whole unstable slope, rock mass strength and newly formed fractures. The role of the fracturing pattern in the evaluation of the slope progressive failure is often not fully

appreciated, given the difficulty in the identification and mapping of newly formed fractures and for this reason gravity-induced joints often remain undetected. The fracturing pattern of the investigated slope should always be compared with the joint distribution of surrounding rock masses considered as stable. This comparison allows for the identification of possible additional joint sets that is proof of higher internal subdivision of the unstable rock mass, also including gravity-induced fractures.

During field investigations of a potential unstable slope susceptible to failure the surveyor must pay particular attention to over-stressed zones of the slope where rock mass damage concentrates, such as at the tips of large pre-existing discontinuities as well as at the toe of the slope and, wherever present, at the lateral constraining margins. In these localized zones, gravity-induced fracturing can initiate and propagate up to coalescing and forming distinct rupture surfaces. Gravity-induced joints can be differentiated on the field from those of tectonic origin on the basis of some geometrical features, in particular persistence and joint roughness (Table 3). Newly formed fractures caused by local tensile and shear stresses have typically low persistence and owing to the coalescence process they terminate against pre-existing, through-going joints. Gravity-driven joints have irregular profiles, even with abrupt changes in the main direction caused by irregularities in the matrix of the intact rock. The identification of gravity-induced fractures in critical zones of the unstable slope represents a major clue for the rock mass damage process related to the progressive development of a fully formed rupture surface that may eventually lead to the slope failure.

Finally, the present paper emphasizes the importance of assessing a well constrained engineering–geological model of the unstable slope prior to carrying out any slope stability analysis. A proper evaluation of the slope failure mechanism and the related rock mass damage process should lead to a preliminary assessment of the stability condition of the investigated slope which should be made on the basis of the geomechanical evidence. The detailed investigation of site conditions and the evaluation of the mechanical processes driving the instability should help choose the most effective calculation approach and numerical tool when analyzing the specific rock slope stability problem (i.e. limit equilibrium method, continuum/discontinuum numerical modeling). As Hungr et al. (2005) stated: “[...] it must always be emphasized that numerical modelling is only a tool and not a substitute for critical thinking and engineering judgment.”

**Acknowledgements** The authors wish to thank the Civil Protection of the Friuli Venezia Giulia Region for the useful slope monitoring data provided. The authors would also like to acknowledge the anonymous reviewers for their help in improving the paper.

## Compliance with Ethical Standards

**Conflict of interest** The authors declare that they have no conflict of interest.

## References

- Abele G (1974) Bergstürze in den Alpen: ihre Verbreitung, Morphologie und Folgeerscheinungen. Wissenschaftliche Alpenvereinshefte 25, München
- Abele G (1994) Large rockslides: their causes and movement on internal sliding planes. *Mt Res Dev* 14:315–320
- Agliardi F, Crosta GB, Meloni F, Valle C, Rivolta C (2013) Structurally-controlled instability, damage and slope failure in a porphyry rock mass. *Tectonophysics* 605:34–47
- Aydin A, Basu A (2005) The Schmidt hammer in rock material characterization. *Eng Geol* 81:1–14
- Barla G, Antolini F, Barla M, Mensi E, Piovano G (2010) Monitoring of the Beauregard landslide (Aosta Valley, Italy) using advanced and conventional techniques. *Eng Geol* 116:218–235
- Barton N, Bandis S (1990) Review of predictive capabilities of JRC-JCS model in engineering practice. In: Barton N, Stephansson O (eds) *Proceeding of the international symposium on rock joints*. Balkema, Rotterdam, pp 603–610
- Barton N, Choubey V (1977) The shear strength of rock joints in theory and practice. *Rock Mech* 10:1–54
- Basu A, Aydin A (2004) A method for normalization of Schmidt hammer rebound values. *Int J Rock Mech Min Sci* 41:1211–1214
- Bolla A, Paronuzzi P (2017) Stress-strain modeling to investigate the internal damage of rock slopes with a bi-planar failure. In: Mikoš M, Vilímek V, Yin Y, Sassa K (eds) *Advancing culture of living with landslides—landslides in different environments*. Proceedings of the 4th World Landslide Forum, 29 May–2 June 2017, Ljubljana. Springer International Publishing, pp 397–405
- Bolla A, Paronuzzi P. Numerical investigation of the pre-collapse behavior and internal damage of an unstable rock slope. *Rock Mech Rock Eng* (**Submitted**)
- Bonzanigo L, Eberhardt E, Loew S (2007) Long-term investigation of a deep-seated creeping landslide in crystalline rock. Part I. Geological and hydromechanical factors controlling the Campo Vallemaggia landslide. *Can Geotech J* 44:1157–1180
- Braathen A, Blikra LH, Berg SS, Karlsen F (2004) Rock-slope failures in Norway; type, geometry, deformation mechanisms and stability. *Norw J Geol* 84:67–88
- Brideau M-A, Stead D, Couture R (2006) Structural and engineering geology of the East Gate Landslide, Purcell Mountains, British Columbia, Canada. *Eng Geol* 84:183–206
- Brideau M-A, Pedrazzini A, Stead D, Froese C, Jaboyedoff M, van Zeyl D (2011) Three-dimensional slope stability analysis of South Peak, Crowsnest Pass, Alberta, Canada. *Landslides* 8:139–158
- Buyuksagis IS, Goktan RM (2007) The effect of Schmidt hammer type on uniaxial compressive strength prediction of rock. *Int J Rock Mech Min Sci* 44:299–307
- Carulli GB (2006) Carta geologica del Friuli Venezia Giulia—Scala 1:150,000 con Note Illustrative. Tabacco, Udine, p 44
- Chang K-J, Taboada A, Chan Y-C (2005) Geological and morphological study of the Jiufengershan landslide triggered by the Chi-Chi Taiwan earthquake. *Geomorphology* 71:293–309
- Chigira M (1992) Long-term gravitational deformation of rocks by mass rock creep. *Eng Geol* 32:157–184
- Chigira M (2009) September 2005 rain-induced catastrophic rockslides on slopes affected by deep-seated gravitational deformations, Kyushu, southern Japan. *Eng Geol* 108:1–15
- Cloutier C, Locat J, Couture R, Jaboyedoff M (2016) The anatomy of an active slide: the Gascons rockslide, Québec, Canada. *Landslides* 13:241–258
- Codeglia D, Dixon N, Fowmes GJ, Marcato G (2017) Analysis of acoustic emission patterns for monitoring of rock slope deformation mechanisms. *Eng Geol* 219:21–31
- Cossart E, Braucher R, Fort M, Bourlès DL, Carcaillet J (2008) Slope instability in relation to glacial debuitressing in alpine areas (Upper Durance catchment, southeastern France): evidence from field data and  $^{10}\text{Be}$  cosmic ray exposure ages. *Geomorphology* 95:3–26
- Deng QL, Zhu ZY, Cui ZQ, Wang XP (2000) Mass rock creep and landsliding on the Huangtupo slope in the reservoir area of the Three Gorges Project, Yangtze River, China. *Eng Geol* 58:67–83
- Eberhardt E (2003) Rock slope stability analysis—utilization of advanced numerical techniques. University of British Columbia, Vancouver
- Eberhardt E (2008) The role of advanced numerical methods and geotechnical field measurements in understanding complex deep-seated rock slope failure mechanisms. *Can Geotech J* 45:484–510
- Eberhardt E, Thuro K, Luginbuehl M (2005) Slope instability mechanisms in dipping interbedded conglomerates and weathered marls—the 1999 Ruffi landslide, Switzerland. *Eng Geol* 77:35–56
- Einstein HH, Dershowitz WS (1990) Tensile and shear fracturing in predominantly compressive stress fields—a review. *Eng Geol* 29(2):149–172
- Euser B, Rougier E, Lei Z, Knight EE, Frash LP, Carew JW, Viswanathan H, Munjiza A (2019) Simulation of fracture coalescence in granite via the combined Finite-Discrete element method. *Rock Mech Rock Eng*. <https://doi.org/10.1007/s00603-019-01773-0>
- Fener M, Kahraman S, Bilgil A, Gunaydin O (2005) A comparative evaluation of indirect methods to estimate the compressive strength of rocks. *Rock Mech Rock Eng* 38:329–343
- Ganerød GV, Grøneng G, Rønning JS, Dalsegg E, Elvebakk H, Tønnesen JF, Kveldevisvik V, Eiken T, Blikra LH, Braathen A (2008) Geological model of the Åknes rockslide, western Norway. *Eng Geol* 102:1–18
- Gigli G, Fanti R, Canuti P, Casagli N (2011) Integration of advanced monitoring and numerical modeling techniques for the complete risk scenario analysis of rockslides: the case of Mt. Beni (Florence, Italy). *Eng Geol* 120:48–59
- Hoek E (2007) Practical Rock Engineering. [http://www.rocsience.com/educational/hoeks\\_corner](http://www.rocsience.com/educational/hoeks_corner). Accessed Apr 2019
- Hoek E, Diederichs MS (2006) Empirical estimation of rock mass modulus. *Int J Rock Mech Min Sci* 43:203–215
- Holm K, Bovis M, Jakob M (2004) The landslide response of alpine basins to post-Little Ice Age glacial thinning and retreat in southwestern British Columbia. *Geomorphology* 57:201–216
- Horii H, Nemat-Nasser S (1985) Compression-induced microcrack growth in brittle solids: axial splitting and shear failure. *J Geophys Res* 90(10):3105–3125
- Hungr O, Corominas J, Eberhardt E (2005) Estimating landslide motion mechanism, travel distance and velocity. In: Hungr O, Fell R, Couture R, Eberhardt E (eds) *Landslide risk management*. Proceedings of the international conference on landslide risk management, Vancouver, BC. CRC Press, Taylor and Francis Group, pp 99–128
- ISRM (1978) Suggested methods for the quantitative description of discontinuities in rock masses. *Int J Rock Mech Min Sci Geomech Abstr* 15:319–368
- Jaboyedoff M, Penna I, Pedrazzini A, Baroň I, Crosta GB (2013) An introductory review on gravitational-deformation induced structures, fabrics and modeling. *Tectonophysics* 605:1–12
- Kahraman S, Fener M, Gunaydin O (2002) Predicting the Schmidt hammer values of in situ intact rock from core sample values. *Int J Rock Mech Min Sci* 39:395–399

- Katz O, Reches Z, Roegiers J-C (2000) Evaluation of mechanical rock properties using a Schmidt Hammer. *Int J Rock Mech Min Sci* 37:723–728
- Marcato G, Bossi G, Frigerio S, Mantovani M, Pasuto A, Schenato L (2014) Studio e monitoraggio della situazione di dissesto che interessa il versante sinistro del Tagliamento in corrispondenza del “Passo della Morte”. Relazione Finale, Convenzione protocollo n. PC/2805/CD2. Unpublished Report for the Civil Protection of the Friuli Venezia Giulia Region
- Martinis B (1985) Il lago quaternario di Forni di Sotto (Alpi Carniche). In: In Alto. Cr. Soc. Alpina Friulana, Udine, vol 47, pp 73–83
- Martinis B (1994) Nuovi dati sul lago quaternario di Forni di Sotto (Udine). In: In Alto. Cr. Soc. Alpina Friulana, Udine, Italy, vol. 76, pp 39–44
- McColl ST (2012) Paraglacial rock-slope stability. *Geomorphology* 153–154:1–16
- Nazir R, Momeni E, Jahed Armaghani D, Mohd Amin MF (2013) Correlation between unconfined compressive strength and indirect tensile strength of limestone rock samples. *Electron J Geotech Eng* 18:1737–1746
- Park CH, Bobet A (2009) Crack coalescence in specimens with open and closed flaws: a comparison. *Int J Rock Mech Min Sci* 46:819–829
- Paronuzzi P, Bolla A (2012) The prehistoric Vajont rockslide: an updated geological model. *Geomorphology* 169–170:165–191
- Paronuzzi P, Bolla A (2015a) Gravity-induced rock mass damage related to large en masse rockslides: evidence from Vajont. *Geomorphology* 234:28–53
- Paronuzzi P, Bolla A (2015b) Gravity-induced fracturing in large rockslides: possible evidence from Vajont. In: Lollino G, Giordan D, Crosta GB, Corominas J, Azzam R, Wasowski J, Sciarra N (eds) *Engineering geology for society and territory: landslide processes*. Proceedings of the XII international IAEG congress, 15–19 September 2014, Turin. Springer, pp 213–216
- Paronuzzi P, Bolla A, Rigo E (2016a) 3D Stress–strain analysis of a failed limestone wedge influenced by an intact rock bridge. *Rock Mech Rock Eng* 49(8):3223–3242
- Paronuzzi P, Bolla A, Rigo E (2016b) Brittle and ductile behavior in deep-seated landslides: learning from the Vajont experience. *Rock Mech Rock Eng* 49(6):2389–2411
- Pisa G (1972) *Geologia dei Monti a nord di Forni di Sotto (Carnia Occidentale)*. Carta Geologica—Scala 1:20000 con Note Illustrative. *Giornale di Geologia. Annali del Museo Geologico di Bologna*. Serie 2a, vol XXXVIII, pp 543–688
- Prager C, Zangerl C, Patzelt G, Brandner R (2008) Age distribution of fossil landslides in the Tyrol (Austria) and its surrounding areas. *Nat Hazards Earth Syst Sci* 8:377–407
- Rocscience (2007) RocData (version 4.0). Rocscience Inc., Toronto
- Sandøy G, Oppikofer T, Nilsen B (2017) Why did the 1756 Tjellefonna rockslide occur? A back-analysis of the largest historic rockslide in Norway. *Geomorphology* 289:78–95
- Sturzenegger M, Stead D (2012) The Palliser Rockslide, Canadian Rocky Mountains: characterization and modeling of a stepped failure surface. *Geomorphology* 138:145–161
- Teza G, Marcato G, Pasuto A, Galgaro A (2015) Integration of laser scanning and thermal imaging in monitoring optimization and assessment of rockfall hazard: a case history in the Carnic Alps (Northeastern Italy). *Nat Hazards* 76:1535–1549
- Tomás R, Abellán A, Cano M, Riquelme A, Tenza-Abril AJ, Baeza-Brotons F, Saval JM, Jaboyedoff M (2018) A multidisciplinary approach for the investigation of a rock spreading on an urban slope. *Landslides* 15:199–217
- Tsou C-Y, Feng Z-Y, Chigira M (2011) Catastrophic landslide induced by Typhoon Morakot, ShiaoLin, Taiwan. *Geomorphology* 147:166–178
- Tuckey Z, Stead D (2016) Improvements to field and remote sensing methods for mapping discontinuity persistence and intact rock bridges in rock slopes. *Eng Geol* 208:136–153
- Willenberg H, Loew S, Eberhardt E, Evans KF, Spillmann T, Heincke B, Maurer H, Green AG (2008a) Internal structure and deformation of an unstable crystalline rock mass above Randa (Switzerland): part I—internal structure from integrated geological and geophysical investigations. *Eng Geol* 101:1–14
- Willenberg H, Evans KF, Eberhardt E, Spillmann T, Loew S (2008b) Internal structure and deformation of an unstable crystalline rock mass above Randa (Switzerland): part II—three-dimensional deformation patterns. *Eng Geol* 101:15–32
- Zangerl C, Eberhardt E, Perzlsmaier S (2010) Kinematic behaviour and velocity characteristics of a complex deep-seated crystalline rockslide system in relation to its interaction with a dam reservoir. *Eng Geol* 112:53–67

**Publisher's Note** Springer Nature remains neutral with regard to jurisdictional claims in published maps and institutional affiliations.